Fabrication and Gas Permeation Studies on Polyimide/Layered-Aluminum Phosphate Nanocomposite Membranes

Wojtek S. Krych
Department of Chemical Engineering
Virginia Polytechnic Institute and State University
Blacksburg, VA 24060-0211

Proposal submitted to the faculty of
Virginia Polytechnic Institute and State University
in partial fulfillment of the requirements for the degree of

Master of Science
In
Chemical Engineering

APPROVED:

Dr. Eva Marand, Chair
Dr. Richey Davis
Dr. Ravi Saraf

July 1, 2003
Blacksburg, VA 24060

Keywords: Gas Separations, Nanocomposite Materials, Aluminum Phosphate, Polyimide

Fabrication and Gas Permeation Studies on Polyimide/Layered-Aluminum Phosphate Nanocomposite Membranes

Wojtek Krych

(ABSTRACT)

Polymer – clay nanocomposites have improved thermal, mechanical, and barrier properties when compared with the pure polymer. The objective of this study was to examine if gas separation performance could be improved by introducing a layered nanopourous aluminum phosphate with a large aspect ratio into a polymeric matrix. The aluminum phosphate has eight membered rings, which could potentially serve as a size selective medium. A hexafluorinated polyimide, 6FDA-6FpDA-8%-DABA, was used as the polymeric matrix. The polyimide and the aluminum phosphate were synthesized separately according to well documented procedures. The two materials were blended and fabricated into nanocomposite membranes. The effect of mixing temperature and percentage of layered aluminum phosphate added to the polymer on the permeation properties were examined. These factors had a direct effect on the degree of intercalation and exfoliation of the nanocomposite structure. Transmission FTIR, TEM, DMTA, and X-ray diffraction were used to characterize the morphology, structure, and composition of these nanocomposite films. The permeation properties of the nanocomposite membranes were evaluated using pure gases (He, O_2, N_2, CH_4, CO_2) at 35°C and a feed pressure of 4 atm. In

general, the permeability decreased and the selectivity coefficients increased when adding 10 wt% aluminum phosphate to the polyimide. Furthermore, the membranes showed size selectivity, consistent with the pore size in the layered aluminum phosphate.

Acknowledgments

I would like to thank my adviser, Dr. Eva Marand, for her insight, advice and patience in helping me make this project possible. Without her assistance and encouragement I would not have achieved my goals here at Virginia Tech. I would also like to thank Dr, Michael Tsapatsis, Hae-Kwon Jeong, and Harikrishnan Ramanan, from the University of Massachusetts for their help in this project as well. In particular, I would like to thank Hae-Kwon Jeong for his assistance in the synthesis of the layered aluminum phosphate and X-ray diffraction analysis, and I am grateful to Harikrishnan Ramanan for the TEM images. Thanks also to Todd Pechar for being a helpful lab mate.

Also, I would like to thank the National Science Foundation for financial support of this project.

Table of Contents

List of Figures

List of Tables

Chapter 1 Literature Review

1.1 Introduction

Polymeric membranes used for gas separations have come a long way in the past twenty years. In particular new materials with improved membrane properties have addressed separations such as nitrogen from air, carbon dioxide from methane, and the recovery of hydrogen from process streams[1-4]. However, there is still room for improvement in order to realize commercial success. Although inorganic zeolite materials can be highly size selective, membranes are typically made from polymeric materials due to their lower processing cost and their ease of fabrication into hollow fibers. This is a geometry, which maximizes the surface to volume ratio and hence the area of the membrane. Unfortunately, polymers lose their performance at high temperatures, high pressure, and harsh chemical environments unless crosslinked. Also, polymers display a trade-off between permeability and selectivity[4]. Inorganic membranes, on the other hand, made from zeolites, molecular sieves, or silicates exhibit desirable gas separation properties and durability. The draw back with inorganic membranes is

the difficulty and cost of manufacturing them into defect-free high-surface area membranes. Thus, supporting zeolites in a processable polymer matrix is being explored[5]. These materials are called mixed matrix membranes. Numerous studies involving both experimental and theoretical studies suggest that these materials should have improved membrane properties over the pure polymer. Unfortunately, at high zeolite landing, mixed matrix membranes tend to become brittle. Similar to mixed matrix membranes, polymer-clay nanocomposites combine inorganic layers with a polymeric continuous phase. However, the large aspect ratios of the inorganic structures lead to some dramatic changes in material properties not observed in systems with symmetric zeolites.

Previously, several groups have combined inorganics such as silicates, montmorillonite clays, and other silicate-based clays with polymers to form nanocomposite materials[(6-14)]. It was shown that silicates and silicate based clays were successfully combined with polymeric materials and that these new nanocomposite materials improved the following features: A small fraction of silicate filler gave significant improvements in the strength and toughness of the materials[(15-19)]; the composites possessed excellent thermal stability and size stability[(15-19)]; and the composite films possessed excellent "barrier" properties due to the planar orientation of the silicate sheets[(20-22)]. In this study, mixed matrix membranes were constructed from aluminum phosphate and a polyimide, previously synthesized in our lab here at Virginia Tech, in attempts to combine the gas separation properties of the inorganic with the processing properties of the polymeric material[(23-26)]. In particular, the selectivity and permeability change

between gases when the mixing time and percentage of inorganics were varied were the focuses of this study.

1.2 Gas Transport through Polymeric Membranes

In this section, I shall discuss the various models and methods I have used in membrane transport analysis. The Time-Lag Method, Dual Mode Sorption Theory, and Free Volume Theory are all models that represent how a gas is transported through a membrane. The principal model for describing gas diffusion through polymeric materials is the Solution-Diffusion Model .[23-24] The permeability, diffusivity and solubility coefficients through rubbery polymers can be calculated by the Time-Lag Method.[27] Describing the diffusion of gas through glassy polymers is more complex because the molecular chains are not at a state of equilibrium. The Dual Mode Sorption Theory and Free Volume Theory are used to describe sorption in polymers.

1.3 Solution-Diffusion Model

The Solution-Diffusion Model is a widely established concept used to describe the flux through a membrane.[1-2] There are three stages to the diffusion of gas molecules. The penetrant molecule first dissolves into the polymer on the upstream side, then the gas diffuses across the membrane by a concentration gradient and finally it desorbs from the downstream side.[1-2] This model can be

used to explain dialysis, reverse osmosis, pervaporation, and gas permeation. The Solution-Diffusion Model is expressed in terms of the chemical potential, which in the case of gas permeation, is related to the gas concentration gradient within the membrane. The chemical potential gradient can be thermodynamically related to temperature, pressure, and molar concentration.

Fick's First Law can be used to model the transient diffusion through a uniform slab

$$J = -D(C)\left(\frac{\partial C}{\partial x}\right), \qquad (1.1)$$

where J is the flux (cm^3 @STP / cm^2 s), D is the diffusion coefficient (cm^2 /s), C is the concentration of the gas in the polymer (cm^3 @STP / cm^3), and x is the thickness of the membrane (cm). Diffusion occurs in the x-direction only, assuming the concentration gradients in the other directions are negligible. Assuming D is independent of temperature and that the concentration obeys Henry's Law, Equation 1.1 becomes

$$J = -DS\left(\frac{\partial p}{\partial x}\right), \qquad (1.2)$$

where S is the solubility coefficient. At steady-state, Equation 1.2 simplifies to

$$J_s = D \times S\left(\frac{p_f - p_p}{l}\right), \qquad (1.3)$$

where J_s is the flux at steady-state, p_f is the feed pressure, p_p is the permeate (downstream) pressure, and l is the thickness of the membrane. The product of D and S,[1,28] is, P, the permeability which can be substituted into Equation 1.3, resulting in

$$J_s = P\left(\frac{p_f - p_p}{l}\right) = P\left(\frac{f_f - f_p}{l}\right). \qquad (1.4)$$

For modeling real gases, the fugacity of the gas, *f*, may replace the pressures as shown in Equation 1.4. This becomes more important at pressures approaching non-ideal conditions.

1.4 Time Lag Method

The permeability can be separated into kinetic and thermodynamic contributions by the application of the Time Lag Method in the analysis of the permeate pressure as a function of time.[27] The time lag is basically the time required for a gas to permeate through a membrane. The integral technique was applied in this study, which measures the accumulation of the permeate gas (pressure) as a function of time. Figure 1.1 represents typical results used in this method. The data is divided into two sections, the first section represents transient diffusion and the second steady-state diffusion.

The time lag is the extrapolation of the steady-state region to the x-intercept, as indicated by the θ in Figure 1.1. The flux can be written in terms of the slope of the steady-state region, which can be represented as

$$J_s = \frac{Slope}{RT} \times \frac{V}{A}\left(\frac{22414\ cm^3(STP)}{mol}\right), \qquad (1.5)$$

R is the gas constant, *T* is the temperature, *V* is the permeate volume, and *A* is the active area of diffusion.[26] Equation 1.6 shows *P* as a function of the slope of

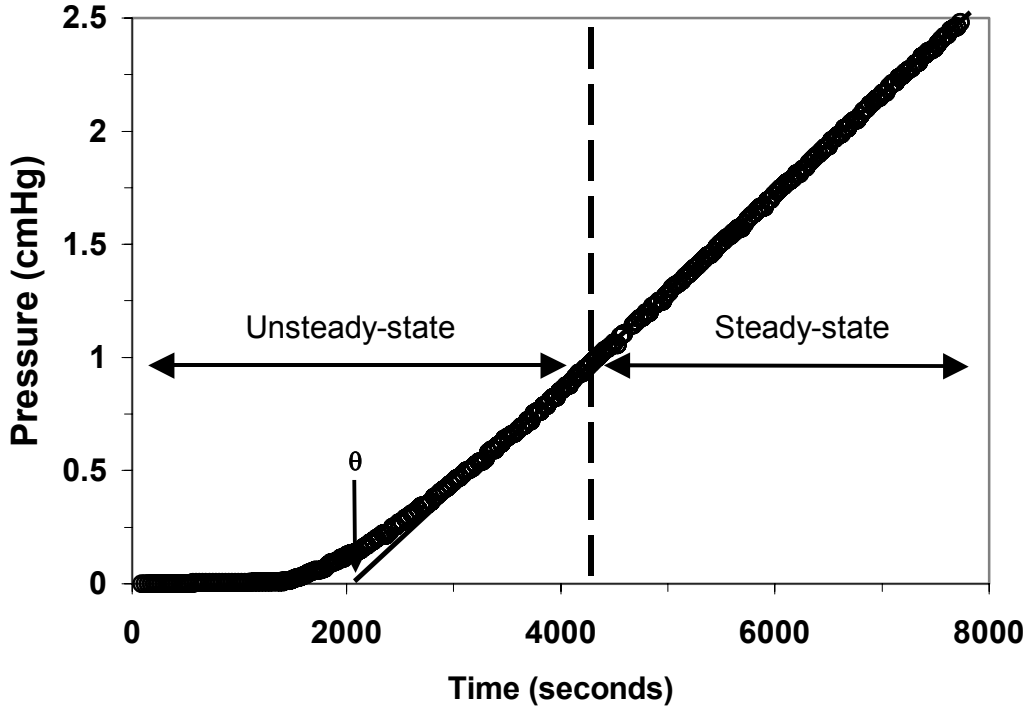

Figure 1.1. Sample results from a gas permeation test using the Time Lag Method.

steady-state diffusion which is a combination of equations 1.4 and 1.5; *P,* in this case, is normalized to the differential pressure and membrane thickness.

$$P = \frac{Slope}{RT} \times \frac{V}{A} \left(\frac{22414\ cm^3(STP)}{mol} \right) \times \left(\frac{l}{p_f - p_p} \right). \qquad (1.6)$$

An assumption that is made for this method is that the permeate pressure, p_p, remains negligible throughout the entire permeation process. If the permeate pressure does not remain negligible, then the flux will begin to level off as a function of time and a different boundary condition will need to be specified, resulting in a more complex relationship.[29] The permeability coefficient is typically reported in the units of Barrer, which is defined in Equation 1.7.

$$1\,\text{barrer} = \frac{10^{-10}\,\text{cm}^3\,(\text{STP}) \cdot \text{cm}}{\text{cm}^2 \cdot \text{s} \cdot \text{cmHg}} \qquad (1.7)$$

Applying Fick's Second Law, shown in Equation 1.8, the diffusion coefficient, can be calculated from the time lag.

$$\frac{\partial C}{\partial t} = D \frac{\partial^2 C}{\partial x^2} \qquad (1.8)$$

The following boundary conditions are assumed to solve Equation 1.8:

$t < 0$	$0 \le x \le l$	$C = 0$
$t \ge 0$	$x = 0$	$C_f = Sp_f$ = constant
$t \ge 0$	$x = l$	$C = 0$

Solution to the partial differential equation, Equation 1.8, with the above boundary conditions is given by Equation 1.9, where Q is the total amount of gas permeating through the membrane, C_f is the concentration at the feed side and t

is time. One-dimensional flow through a membrane is modeled by this equation assuming that D is independent of temperature and concentration.

$$\frac{Q}{l\,C_2} = \frac{Dt}{l^2} - \frac{2}{\pi^2}\sum_{n=1}^{\infty}\frac{(-1)^n}{n^2}\exp\left(-\frac{Dn^2\pi^2 t}{l^2}\right) \qquad (1.9)$$

When *t* goes to infinity, representing steady-state diffusion, the summation approaches 1/6, simplifing Equation 1.9 to:

$$\frac{Q}{l\,C_2} = \frac{Dt}{l^2} - \frac{1}{6}. \qquad (1.10)$$

Rearranging Equation 1.10 results in

$$Q = \frac{DC_2}{l}\left(t - \frac{l^2}{6D}\right) = \frac{DC_2}{l}\left(t - \theta\right) \qquad (1.11)$$

where $\theta = l^2/6D$. The solubility coefficient (*S*) can be calculated by equation 1.12 if *P* and *D* are known along with $P = D \times S$.

$$S = \frac{P}{D} \qquad (1.12)$$

The presence of an inorganic component with completely different diffusion and sorption properties than the pure polymer will change the boundary conditions. Therefore, we define an effective P, S, and D. In summary,

$$P = \frac{Slope}{RT} \times \frac{V}{A}\left(\frac{22414\ cm^3(STP)}{mol}\right) \times \left(\frac{l}{p_f - p_p}\right) \qquad (1.13)$$

$$D_{eff} = \frac{l^2}{6\,\theta} \qquad (1.14)$$

$$S_{eff} = \frac{P}{D_{eff}} \qquad (1.15)$$

In addition, for pure gas permeation experiments, ideal selectivity can be defined as

$$\alpha^* = \frac{P_A}{P_B}. \qquad (1.16)$$

Perry *et al.* have explored the theoretical effects of incorporating non-permeable inclusions, such as mica flakes, into a polyimide matrix on the diffusive time lag to construct a nanocomposite polycarbonate film.[30] It was demonstrated that the mica flakes must be oriented with their long axis perpendicular to the gas flow in order to force the gas to take a longer path around the obstructing particles resulting in lower permeabilities and higher selectivity coefficients. Also, a theoretical model relating the mica loading and size of flakes to increases in diffusion time lag was presented, which correlated well with experimental data. The model is shown in Equation 1.17.

$$\theta(\text{with flakes}) = \theta(\text{without flakes}) \times (\alpha)^2 \times (\phi)^2 \qquad (1.17)$$

θ is the time lag, α is the aspect ratio of the flakes, and ϕ is the volume % of flakes in the polymer. For example Equation 1.17 can be used to show that the diffusion time lag can be increased nearly 25 times with a mica loading of 25% and size aspect ratio of 20. These results were attributed mainly to increasing the tortuousity of the path of diffusion and to illustrate that the diffusion time lag can be altered by the presence of inclusions in the polymer. These particular results are promising for improving nanocomposite membranes by creating a barrier.

Equation 1.18 has been developed by Cussler to predict the permeability through such non-permeable layered sheets when incorporated in a nanocomposite [30].

$$P_{eff,\,i} / P_{p,\,i} = [1+\alpha^2 \phi^2 /(1-\phi)]^{-1} \qquad (1.18)$$

$P_{eff,\,i}$ is the effective permeability of species i, $P_{p,\,i}$ is the experimental permeability of species i, α is the aspect ratio, which is estimated at 1000 in this case and, ϕ is the volume fraction of the impermeable layer in the nanocomposite, which is 5% and 10% in this case. Equation 1.18 is most useful when these strongly anisotropic layered sheets are arranged with their short axis perpendicular to the film axis. Therefore, as the experimental permeability gets closer to the effective permeability, the more the layers are arranged perpendicular to the gas flow resulting in lower permeability. Similarly, Equation 1.19 has been developed by Yano, Usuki, and Okada to predict the permeability through polyimide-clay hybrid films [9].

$$P_c/P_p = 1/(1+(L/2W)V_f) \qquad (1.19)$$

P_c is the permeability coefficient of the composite, P_p is the permeability coefficient of the polymer matrix, L is the length of a plate which, is assumed to be 1000, W is the with of a plate, which is assumed to be 1, and V_f is the volume fraction of the plates. Equation 1.19 has been used to model water vapor permeating through polyimide-clay hybrid films, and assumes that all the clays are arranged perpendicular to the gas flow direction.

Up to now there are no published theoretical models for predicting the time-lag in heterogeneous systems consisting of permeable filler materials in a permeable matrix.

1.5 Gas Transport through Hybrid Membranes

Both the Time-Lag Method and the Dual Mode Sorption Theory have to be applied with caution when describing the gas transport through these hybrid membranes, because there is heterogeneity in both the polyimide and the inorganic material. The Time-Lag Method was originally developed for rubbery polymers, and the Dual Mode Sorption Theory describes glassy polymers based on only two methods of sorption. Four methods of sorption, however, have been identified for these hybrid systems: i) gas molecules “dissolved” into the amorphous polymer matrix (Henry’s Law) ii) gas molecules adsorbing in to “holes” in the glassy polymer (Langmuir) iii) gas molecules adsorbing in to “holes” in the organosilicate network and iv) and gas molecules adsorbing in to “holes” at the polyimide- inorganic interface. Sorption isotherms will provide little information pertaining to the mode of transport in these membranes because there are so many unknown variables. Therefore, the focus is on transient permeation testing whose analysis assumes that sorption simply follows Henry’s Law.

The Time Lag Method was chosen for this study because of its sound fundamental basis and ease of data collection. The values of permeability are

precise for these nanocomposite membranes, however, the diffusivity and solubility coefficients are not exact in absolute terms. The basis of this assumption originates from a study by Paul and Kemp, who stated that increasing filler content will cause increases in the time lag but will reveal only minor effects on the steady-state permeability for a rubbery polymer containing adsorptive filler materials.[31] Zimmerman *et al.,* in a different study, compared the diffusion coefficients determined by various experimental techniques and summarized that the Time Lag Method did not accurately represent the true diffusion coefficient, however, the ratios giving diffusivity and selectivity were comparable with those measured by other methods.[32] The belief is that the solubility and diffusion coefficients from permeability measurements are useful for making qualitative comparisons between the pure polymeric membranes and the nanocomposite membranes.

To compare the performance of these nanocomposite materials, the permeability and selectivity will be plotted on a boundary diagram, as founded by Robeson.[4] After conducting an extensive literature search, Robeson plotted the tradeoff between ideal gas selectivity and gas permeability of polymers for several gas pairs (He, H_2, O_2, N_2, CH_4, CO_2).[4] He concluded that a trade off exists between the selectivity coefficient and the permeability, and that an empirical “upper bound” exists for most commercially viable membranes that needs to be surpassed. Freeman later substantiated Robeson’s upper bound with a theoretical explanation relating the slope of the line to molecular parameters, such as molecule size, interchain spacing and polymer backbone

stiffness.[33] A perfect fit was not achieved between the theoretical model and the empirical upper bound, but the fundamental and simple theory did merit an upper bound for simple gas pairs.

1.6 Polymer – Inorganic Nanocomposite Materials

Polymer nanocomposites poses properties that offer significant commercial potential. Polymer nanocomposites are defined as the combination of a polymer matrix resin and inclusions that have at least one dimension (i.e. length, depth, or thickness) on the nanometer scale [34]. Nanocomposite materials incorporating different types of inorganics with polymers have been successfully synthesized, fabricated and characterized [(6-14)]. Some of these organic – inorganic systems include; polymer - cobalt, nickel, copper, or other metal combinations. None of these nanocomposites have been fabricated for gas separation purposes, instead the main research of these materials focuses on improvements in strength and toughness. It has been shown time and again, that a small percentage of inorganic material can increase physical properties dramatically [(6-14)].

There are several different methods for processing polymer-clay nanocomposites. Exfoliation-adsorption is a process where the layered inorganic material is exfoliated into single layers using a solvent in which the polymer is soluble. The layered sheets become easily dispersed in an adequate solvent due to the weak bonds between the layers. The polymer then adsorbs onto the

delaminated sheets and when the solvent evaporates, the sheets reassemble, sandwiching the polymer in between resulting in a multi-layer structure. In situ intercalative polymerization is the technique where the layered inorganic material is swollen within the liquid monomer so the polymer formation can occur between the intercalated sheets. The polymerization is initiated either by heat, radiation, the diffusion of a suitable initiator, or by an organic initiator[6-14]. Blend intercalation, the process used in this research, is performed by mixing the inorganic material with the polymer matrix in a solvent in the dissolved state. The polymer protrudes into the interlayer space and forms either an intercalated or an exfoliated nanocomposite. The polymer, solvent, and inorganic material must be very compatible if this process were to be used[6-14]. Finally, template synthesis is the process where the inorganic material is constructed in situ in an aqueous solution containing the polymer and the inorganic building blocks to form double-layered hydroxide based nanocomposites. In this technique, the polymer aids the nucleation and growth of the inorganic host crystals by getting trapped within the inorganic layers as they grow. This is the least used technique[6-14].

Reinforcing polymers with layered silicates is common today in the production of various coatings and packaging materials. For example, the addition of 4.7 wt% montmorillonite clay to nylon-6 increased the tensile strength from 68.6 MPa to 97.2 MPa and the modulus from 1.11 GPa to 1.87 GPa when going from the pure polymer to the nanocomposite [35]. The addition of 12.6 wt% of montmorillonite clay to polymethyl methacrylate showed a tensile stress improvement from 53.9 MPa to 62.0 MPa, and an addition of 5 wt% of clay to

polypropylene improved tensile stress from 31.4 MPa to 39.5 MPa. When the clay content is increased from zero in nylon-6 to 2.5 wt% and 5 wt%, the maximum degradation temperature increases from 452 to 489.2 and 493.5 respectively. These are substantial changes in physical properties, which cannot be explained with simple mixing theories, but which are directly related to the high aspect ratio of the silicate layers. Significant enhancements in reinforcement, thermal endurance, electrical conductivity, flame resistance, abrasion resistance, and improved barrier properties have been observed. Besides improved physical properties, nanocomposite materials are also extruded with more ease and molded to near-final shape with simpler methods [36]. Thus, interest in new nanoscale fillers, synthesis approaches, processing techniques, morphological characterization, structure-property relationships, and rheology is growing at a rapid rate.

Although significant progress has been made in developing polymer nanocomposites with polymer matrices and inorganic materials, the development of property models seems to be the remaining challenge. Progress in the engineering of nanocomposites has remained largely empirical because of the lack of such models [37]. Although permeability of these nanocomposites can be predicted to an extent, the absence of property models has made predicting material limits or maximum performance of these nanocomposites very difficult.

1.7 Theory of Intercalation and Exfoliation

When a polymer is blended with layered clay, intercalates, exfoliates, or a combination of the two may result. Intercalates are obtained when the polymer is between the clay layers which result when layer spacing is increased; attractive forces between the clay layers cause the layers to arrange in regularly spaced stacks or tactoids. Exfoliates are formed when the layer spacing increases to the point where there is no longer sufficient attraction between the clay layers to cause a uniform layer spacing [37 - 39]. For a true exfoliate to result, the clay layers must be randomly dispersed throughout the composite and this will depend on thermodynamics, interactions of the clay layer, the cation residing between the layers, and the polymer matrix [38]. Figure 1.2 depicts the intercalation and exfoliation morphology of inorganic sheets and a polymer. Since the improvement in physical properties of the nanocomposites scales with the degree of dispersion of the nanoparticles, exfoliated clay structures are desired [37 - 39].

Giannelis and co-researchers have explained the thermodynamic driving force behind exfoliation [40-43]. It is known that entropy is gained in the translational freedom of many desorbed molecules from the host galleries. Thermogravometric analysis proves that the organosilicate nanocomposites do not undergo any weight loss when thermal energy is added, and this suggests that there is no release of water or other small molecules from the nanocomposite samples during heating. Therefore, the entropic penalty for

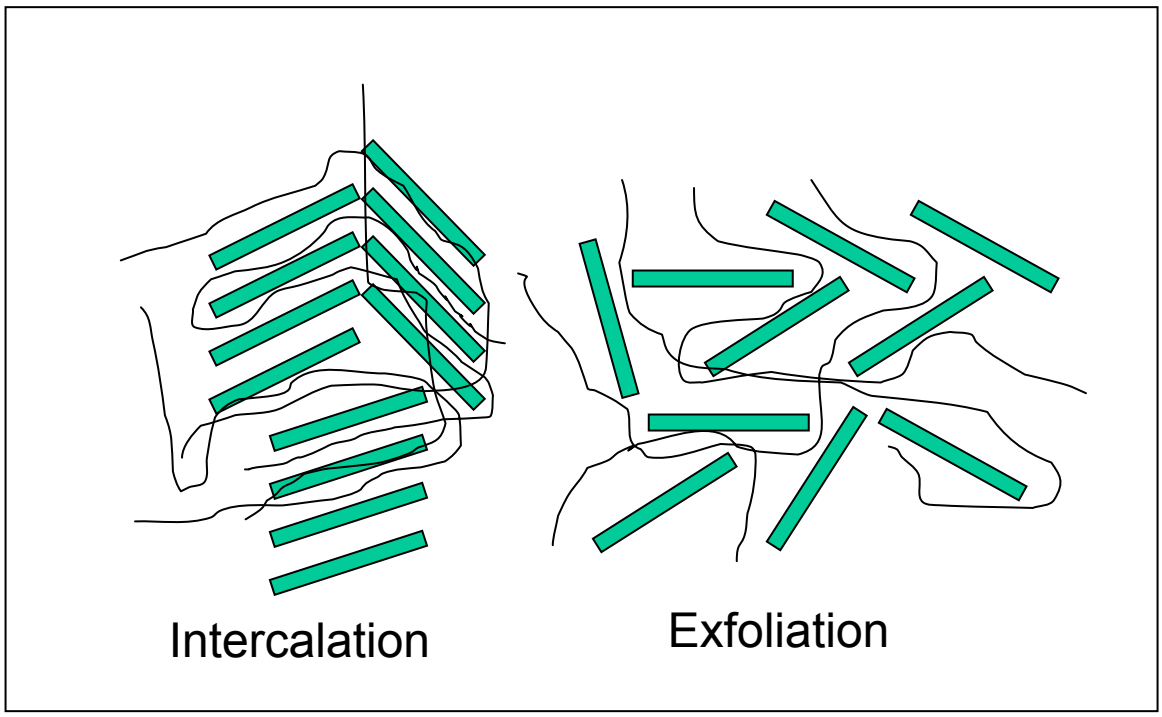

Figure 1.2. Schematic of intercalation and exfoliation.

confinement of the polymer must be overcome by increasing the interaction energy between the polymer and the clay sheets, theorizing that direct intercalation is enthalpically driven.

X-ray diffraction studies have been carried out to prove that intercalation takes place. Transition electron microscopy (TEM) physically shows the sheets of inorganic clay material on a nanometer scale [6-14]. TEM images clearly show "whiskers" on the nanometer scale that represent single sheets of inorganic material; these sheets are several times longer than wider and organize in no particular direction [6-14].

Exfoliated nanocomposites are desired when lowering permeability. It has been discovered that the layered nature of exfoliated clays in polymers dramatically reduces the permeability of gases through the composite. Two mechanisms have been proposed for this altercation in permeability behavior; the first involves the tortuous path of the diffusing molecule and the second involves the large interfacial volume of the nanocomposite [39]. The tortuous path mechanism theorizes that a clay sheet is non-permeable and that the diffusing species has to change direction repeatedly as it permeates through the nanocomposite material and therefore a much longer diffusion path length results[39-41]. The large interfacial volume mechanism theorizes that the large surface area of exfoliated clays cause the majority of the polymer to lie close to the clay-polymer interface, which restricts the mobility of the polymer molecules and thus any molecules attempting to diffuse through the polymer. The later

concept has been supported by research on small molecule interactions between clays and polymers by proving that polymer mobility is reduced at the interface[39-41]. It is, however, probable that both mechanisms are involved in reducing permeability, although, it is not known how much of each effect contributes to the reduction in permeability.

It has been shown that permeability properties are reduced drastically when adding longer clay sheets at constant 2 wt% clay to a polyimide [44]. The permeability coefficient decreased from 0.98 to 0.79, 0.45, and 0.1 when the length of the clay increased from 460 angstroms for hecrite to 1650 angstroms for saponite, 2180 angstroms for montmorillonite, and 12300 angstroms for synthetic mica. This 2 wt % addition of synthetic mica brought the gas permeability coefficient to a value less than one-tenth of that of the original value proving that length does matter. Such effects on in permeability can be explained by the aggregation of hectrite and nonhomogeneous dispersion of saponite in the hybrids [6-14]. As free hydroxide groups of mica mineral are substituted by fluorine in synthetic mica, water vapor is repelled from the organophilic mica resulting in larger gas barrier properties of the mica hybrid and a smaller relative permeability coefficient [42-44].

Chapter 2 Experimental

2.1 Polyimide Synthesis

All previous synthesis of the polyimide, 6FDA-6FpDA-DABA, used in this study was performed by Dr. Chris Cornelius.[23-26] Attempts to repeat the synthesis yielded polymers with low molecular weight, which could not be used in the fabrication of nano-composite membranes. However, a brief summary of the procedure is given, along with some explanations for the low molecular weight.

700ml of NMP (1-Methyl-2-Pyrrolidinone) and 250ml of DCB (o-Dichlorobenzene) were dried by stirring in phosphorus pentoxide for 24 hours and then distilling it under vacuum. Stoichiometric amounts of 6FDA (4,4'-(Hexfluoroisopropylidene)diphthalic Anhydride) and 6FpDA (4,4'-(Hexfluoroisopropylidene)dianiline) were weighed out and also dried by placing them in an oven under vacuum for at least 4 days at 100°C. Next, stoichiometric amounts of NMP, DCB, 6FDA, and 6FpDA were added to a previously dried 1000ml round bottom flask to form a polyamic acid solution. After allowing this polyamic acid solution to stir for 24 hours at room temperature

under a nitrogen purge, a polyimide, 6FDA-6FpDA, was formed by thermal imidization. Thermal imidization occurred when the polyamic acid solution was stirred for another 24 hours at 180°C under nitrogen purge. Any water that is formed during cyclodehydration of the polyamic acid solution at 180°C was removed with the modified Dean-Stark trap and Allhin condenser. Water forms a low boiling azeotrope with DCB and must be removed. The equipment set up for the solution imidization technique and the formation of 6FDA-6FpDA are depicted in Figures 2.1 and 2.2 respectively.

At this point it was desired to add DCB (3,5-Diaminobenzoic Acid) to the polyimide. This was done by first taking the 6FDA-6FpDA and allowing it to cool back to room temperature. The desired amount of DCB is added stoichiometricaly to the polyimide solution; in this case 8% was desired. After addition, the solution was stirred at room temperature for 24 hours and then again stirred at 180°C for 24 hours, just like before. Next, 6FDA-6FpDA-DABA was formed by the solution imidization technique as represented by Figure 2.3. The 6FDA-6FpDA-DABA was cooled and filtered with a 5 μm nylon filter and then precipitated out of the solution of NMP and DCB using methanol.

The actual synthesis I conducted was unsuccessful because a sufficient molecular weight was not achieved. It is possible that the stoichiometric amounts of 6FDA and 6FpDA were off when the chemicals were weighed out or that water got into the reaction thus resulting in a low molecular weight polymer. Water entered the reaction by either not having enough nitrogen purge through the

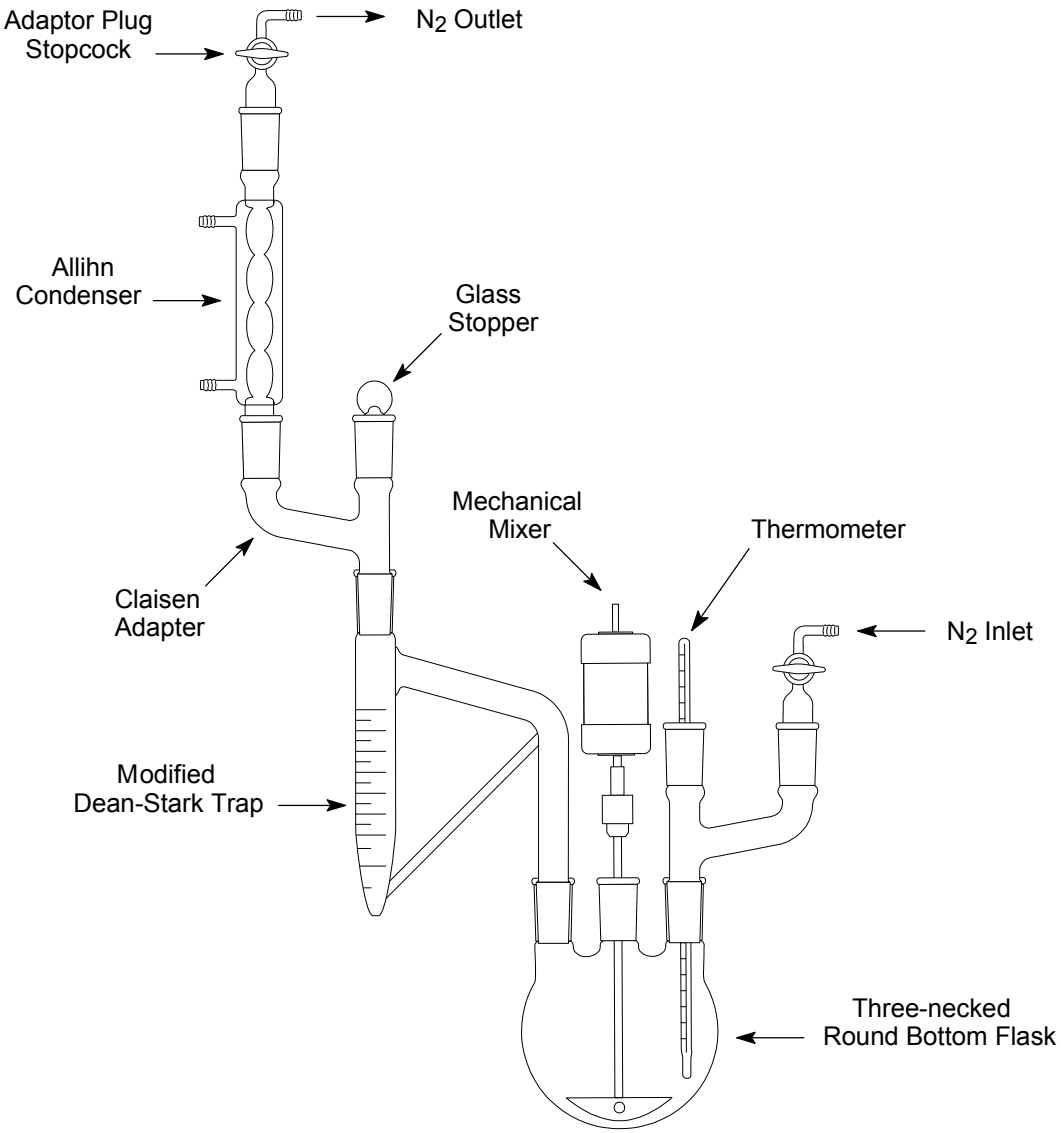

Figure 2.1. Apparatus for the solution imidization technique

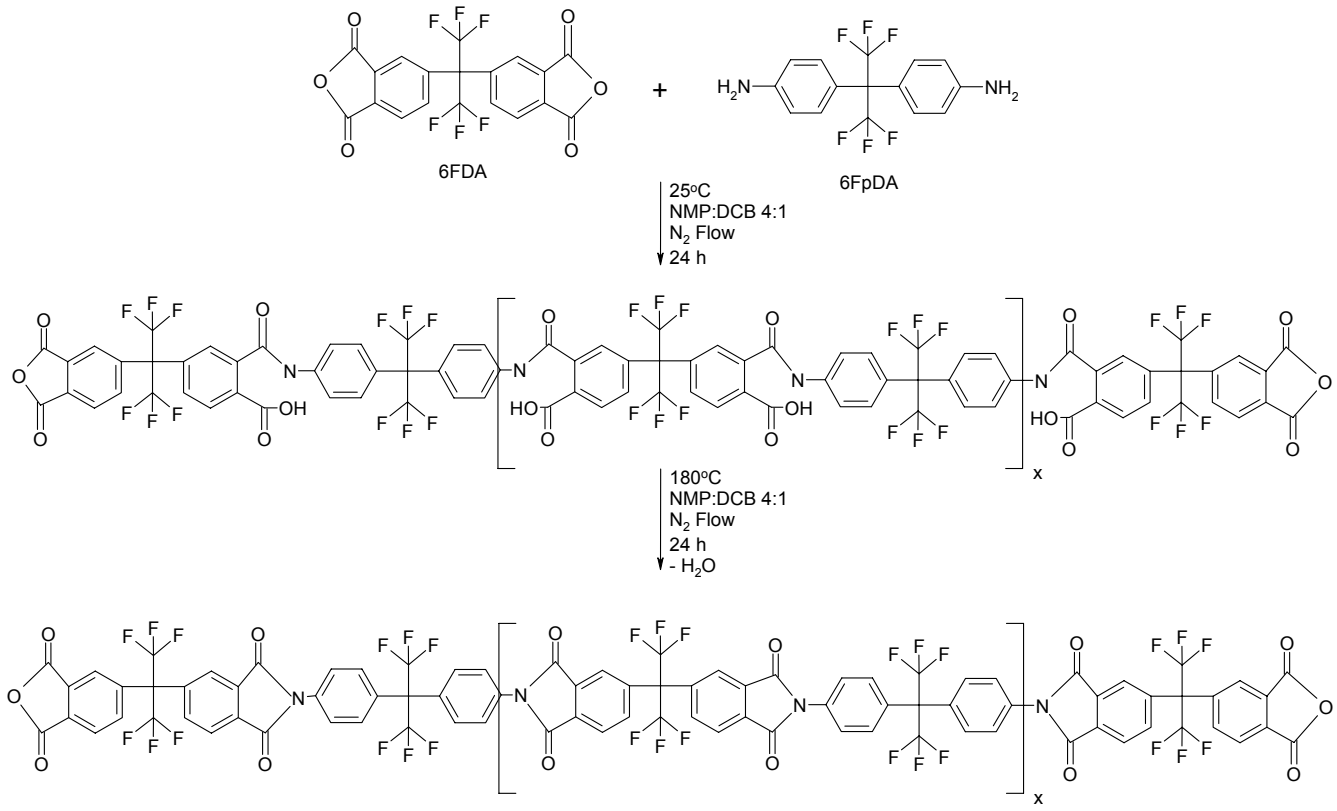

Figure 2.2. 6FDA-6FpDA formation via solution imidization technique

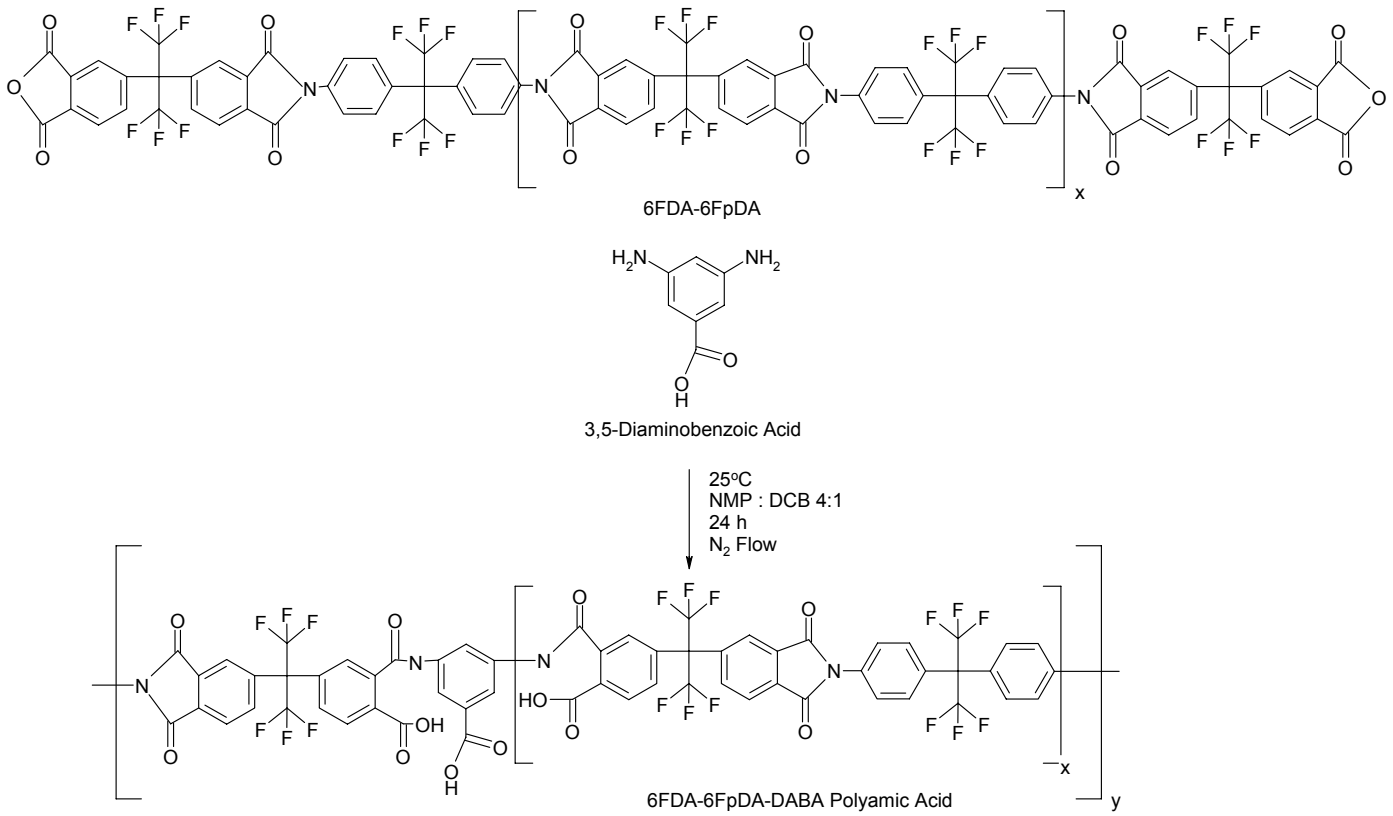

Figure 2.3 6FDA-6FpDA-DABA formation via solution imidization technique

apparatus allowing water to accumulate or by not being removed by the modified Dean-Stark trap as should have been.

2.2 Layered AluminumPhosphate Synthesis

A typical synthesis consisted of adding aluminum triisopropoxide (8.0g) to a ethylene glycol (66.0g) and n-butanol (80.0g) solution. This was allowed to mix and disperse for 48 hours; a white low viscous gel solution was formed. Next, ethylamine (34.72g, 70 wt% in water) and phosphoric acid (13.44g, 85 wt% in water) were added. This mixture was stirred until homogeneous, sealed in Teflon-lined autoclaves with a filling rate at 70% (volume), and heated for 13 days at 180°C under autogeneous pressure [45]. The solution that was removed was in the form of crystals in a viscous slurry and was vacuum filtered and washed with water. This layered aluminum phosphate (ALPO) is constructed of sheets with a 4 x 6 x 8 network with a pore size of ca. 3.8 x 6.0 Å as shown in Figure 2.4[48].

The as-synthesized layered ALPO was then taken and swelled via a cation exchange. This was done by combining as synthesized ALPO (0.2g), cetyltrimethylammonium chloride (40g, 25 wt% in water), and tetrapropylammonium hydroxide (1.5g, 40 wt% in water) and allowing it to heat in an oil bath for 16 hours at 80°C [46,47]. The solution was then vacuum filtered and washed with water as before. The actual swelling takes place when the

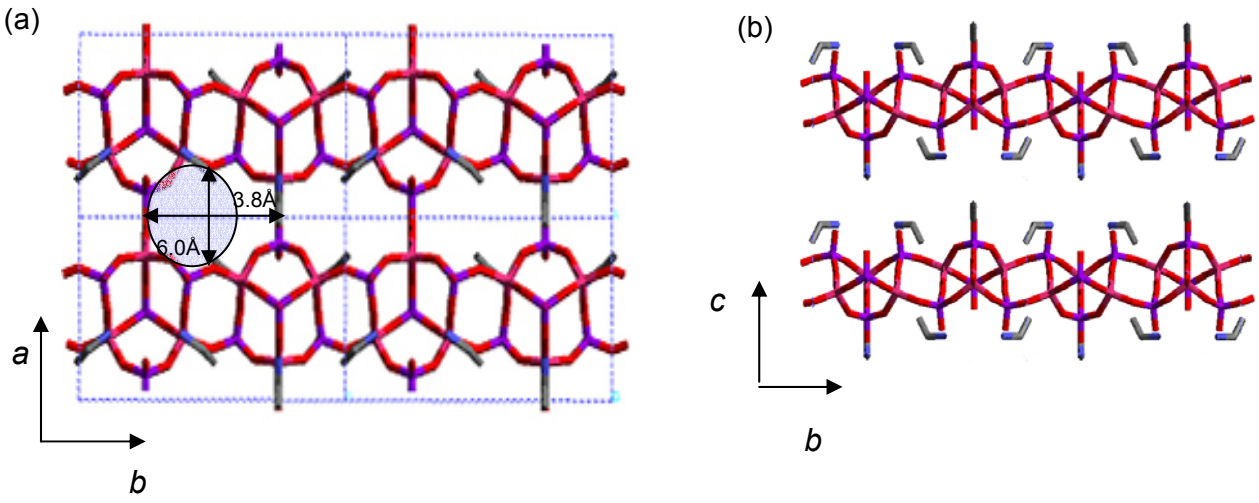

Figure 2.4. Crystal structure of ALPO (a) projection along c axis and (b) projection along a axis.

ethylamine cation gets replaced with the cetyltrimethylammonium cation. The purpose of swelling is important for two reasons. First, to make the ALPO layers hydrophobic so that it is more compatible with the hydrophobic polyimide, and second to expand the interlayer spacing so the polyimide may better access, protrude, and eventually exfoliate the layers.

2.3 Nanocomposite Synthesis and Fabrication

The ALPO - polyimide nanocomposite was constructed by first allowing 1.0g of polyimide (56.1K M_W, 6FDA-6FpDA-8%-DABA) to dissolve into 10ml. of tetrahydrofuran (THF) for 24 hours. This polyimide with 8% DABA was chosen because of its high molecular weight. Layered ALPO crystals based on desired mass percentage, 10% here, of inorganic material were added to this solution and allowed to mix for 7 days so that enough time was allowed for the polymer to protrude into the swollen ALPO layers. After 7 days, the solution was cast into 6.2 cm. diameter muffin Teflon$^{@}$ pans, covered with glass and weighed down, and allowed to sit for 5 or 6 days or until the membranes began to peel from the Teflon$^{@}$. This was done on a flat surface to insure uniform thickness of the membranes. It was of great importance that the beakers, pans, magnetic stir bars, etc. be dry when performing this procedure.

2.4 Annealing Procedure

The films were then placed in a Fisher Scientific vacuum oven at 50°C for 5 hours, heated to 150°C for 5 hours, and then heated to 220°C for 12 hours. The objective of the annealing was to remove all THF before the permeation testing.

2.5 Gas Permeation – General Information

The constant volume method, which utilizes the increase of flux or pressure as a function of time, was used to determine gas permeability. Each test was initiated after the feed, permeate, and membrane sample were degassed to a pressure of 1 to 10 mTorr and until thermal equilibrium reached 35°C.

Pure gas permeation measurements of He, O_2, N_2, CH_4 and CO_2, all at 99.999% purity were carried out. The trials were performed under a feed pressure of 4 atm and a temperature of 30°C. To ensure reproducibility, each membrane was tested three times for each gas and the average results were recorded. The total error for permeability between runs was 4.7%.

2.6 Gas Permeation - Equipment

A schematic diagram of the gas permeation system, with all sections connected with 1/8 OD 316 stainless steel tubing, is shown in Figure 2.5. The

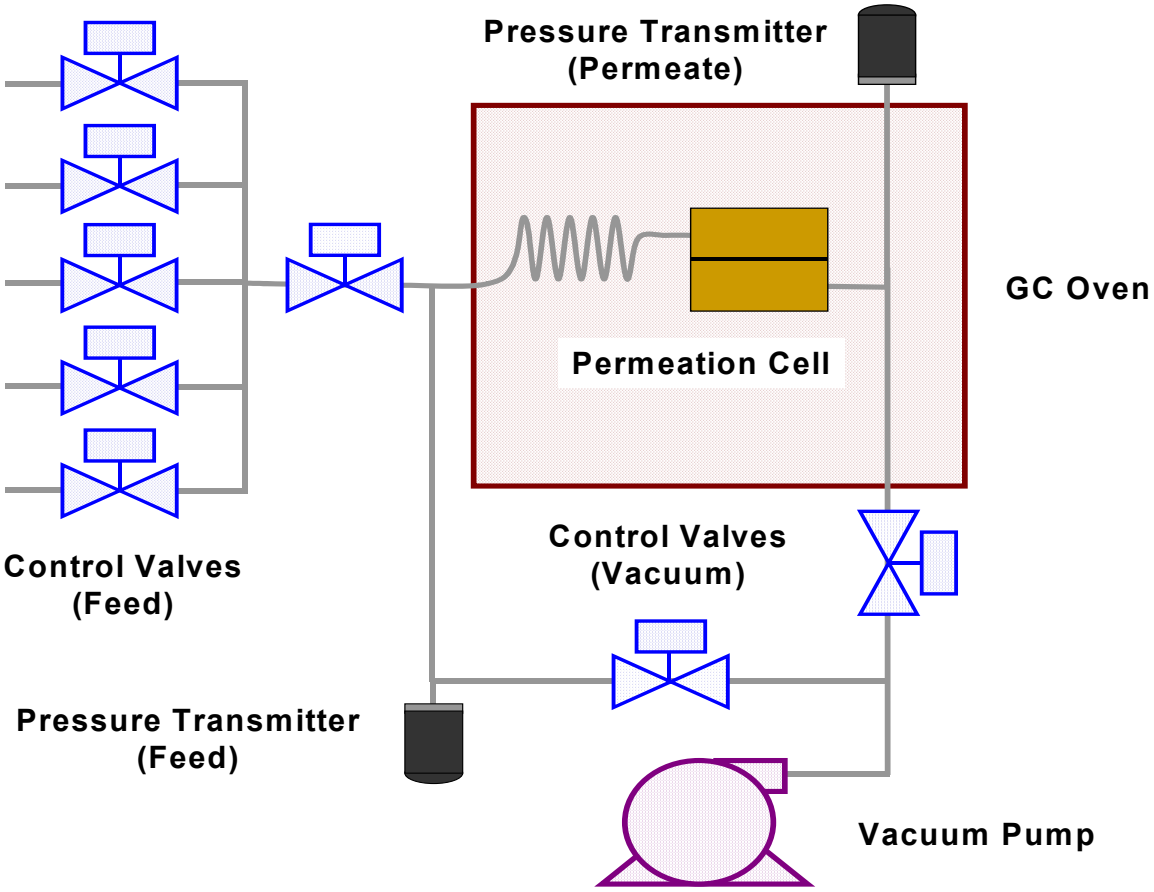

Figure 2.5 Schematic of gas permeation equipment set-up and control scheme.

temperature of the gas permeation process is controlled to 0.1°C with a VEGA 5300 Series gas chromatograph oven. The temperature was monitored and collected via an AC5672 thermocouple card and a type K thermocouple.
A 486DX computer along with a series of pneumatic block valves were used to control the opening and closing of different feed gases, to degas the permeation cell, and to protect the pressure transducer on the permeate section. The permeate pressure was measured via a MKS Baratron® 722A absolute pressure transducer with a range of 0 to 100 Torr and a resolution of 0.1% of full-scale. The feed pressure was measured with a pressure transducer from Validyne Eng. Corp. Northridge that has an opening range of 0-45 atm. The system was degassed with a two-stage vane vacuum pump from Alcatel Corp that is rated for a vacuum of 1 mtorr. The hardware used to interface the computer with graphical interface programming was software from LABTECH.

2.7 Gas Permeation – Cell

Figure 2.6 depicts the 316 custom-designed stainless steel gas permeation cell that was used in this study. This cell was designed for thin membranes measuring approximately 5.0 cm in diameter. A feed half and a permeate half are the two parts that structure the cell, each piece is 10.2 cm in diameter. Two porous 100μm stainless steel sintered disks (manufactured by Mött Corporation) are inserted to provide mechanical support and prevent the membrane from cracking or fracturing. Three radial static seal fluorocarbon

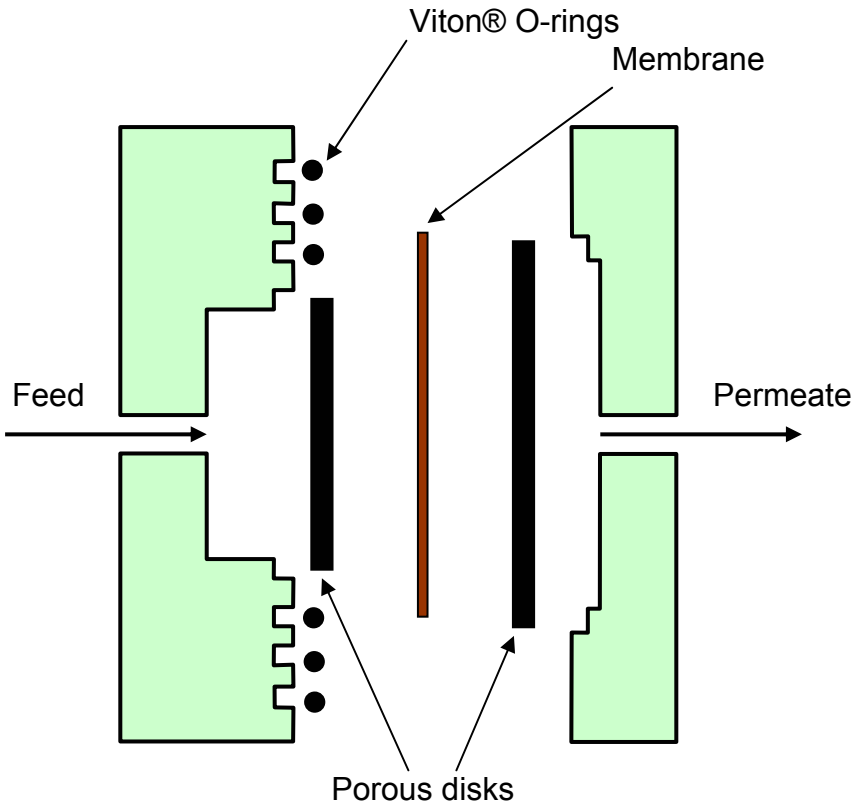

Figure 2.6. Schematic diagram of gas permeation cell.

Viton® Static Seal O-rings are used to seal the membranes and prevent gases from leaking out of the cell. Six ¼" bolts are used to fasten the two cell parts together. The active permeation area is 11.51 cm^2 for gas diffusion.

2.8 X-Ray Diffraction (XRD)

X-ray diffraction patterns were obtained with an x-ray diffractometer (Phillips X'pert) using Cu Kα. The voltage was set at 45KV and the current was 40 mA. Also, the slits were 1°/1° while the step size and scanning speed were .02° and 1.5 sec./step respectively. The wavelength used was 1.56 Å. Figure 2.7 depicts the principle of X-ray diffraction. The figure shows the diffraction from two scattering ALPO layers that are separated by a distance "d"; the d-spacing also known as the interlamellar spacing or the basal spacing (51-54). The wavelength, λ, and incident angle, θ, are also shown. The experimental 2θ value is the angle between the diffracted and incoming X-ray beams; this is the angle that is plotted versus intensity when examining XRD patterns. The points of identical phase for incident and diffracted waves are connected by the wave normals. For total constructive reinforcement to occur between the scattering from these planes, the distance A+B must add up so the wavelength is a whole number; i.e. $n \bullet \lambda$, where n is an integer.[49,50] Constructive interference occurs when Bragg's Law is satisfied which is represented in equation 2.1.

$$n \bullet \lambda = 2 \bullet d \bullet \sin \theta \qquad (2.1)$$

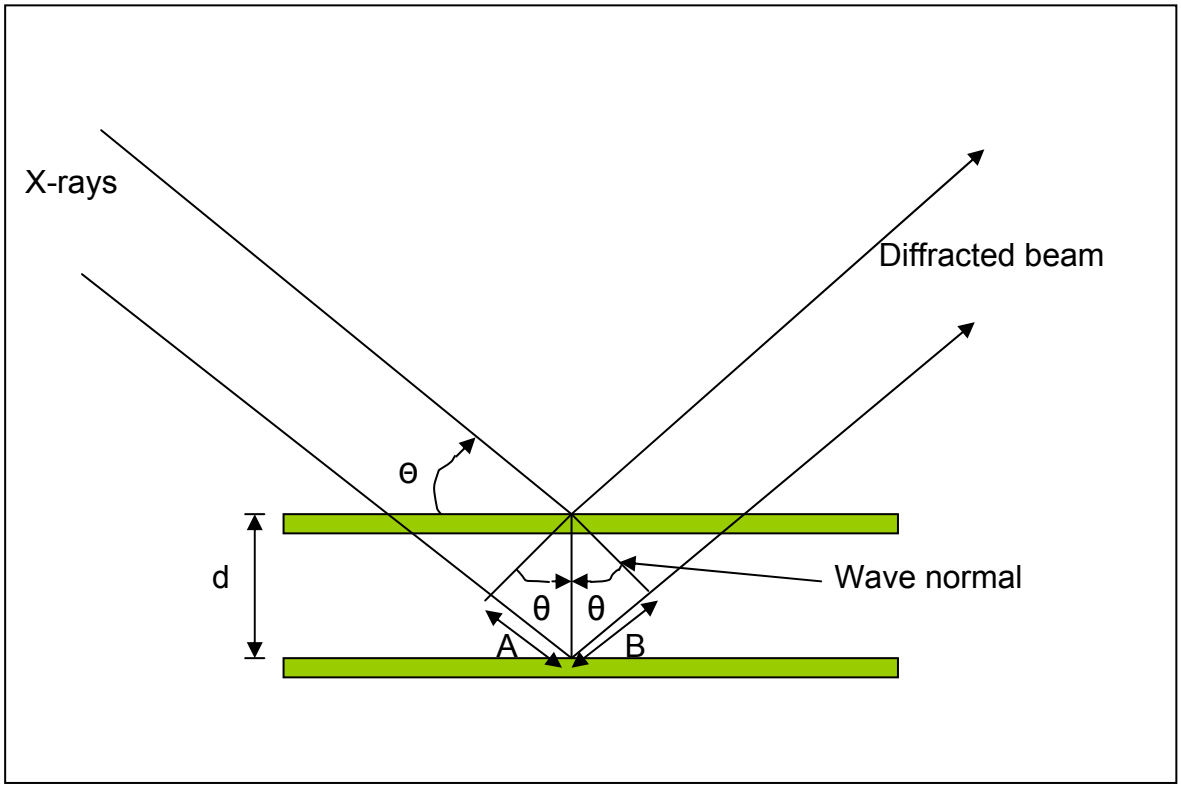

Figure 2.7. Principle of X-ray diffraction.

n is the degree of diffraction, λ is the wavelength, *d* is the basal spacing, and θ is the incident angle. Since the angles opposite to A and B are also θ, $\sin\theta = A/d = B/d$ so that $(A+B) = 2 \cdot d \cdot \sin\theta$. For example, if d_{001}=10Å, then d_{002} = 5Å, d_{003} = 3.33Å etc.

Figure 2.8 is an example of an XRD pattern; this is the XRD pattern for as-synthesized ALPO. The main peak of concern in this pattern is the (001) reflection, which is the basal spacing between two layered ALPO sheets. This peak occurs at 2θ=9.75, which corresponds to a spacing of 9.1Å when applying Bragg's law. The other peaks represent distances between any two atoms i.e. aluminum, phosphate, oxygen etc. The height of the peaks represents the intensity at that angle. In this research the basal spacing, which is represented by the (001) reflection is of most interest because this is the spacing, which will change with polymer intercalation. The other peaks, their intensities, and the distance between them are simply part of a fingerprint to confirm that these particular layered ALPO sheets posses the desired 4 x 6 x 8 network structure. Comparisons of the XRD pattern shown in Figure 2.7 with that from literature indicates a match, hence the correct structure was indeed synthesized[45].

When performing XRD on thin nanocomposite films, a low angle ($2\theta < 9°$ i.e. d>9.8Å) must be used in order to detect the (001) reflection and evaluate the basal spacing between the ALPO layers. When performing XRD on nanocomposite films, a thin film with a large surface area is required to minimize noise in the XRD pattern; typically 0.1 mm for polymers [13,14]. This is done by

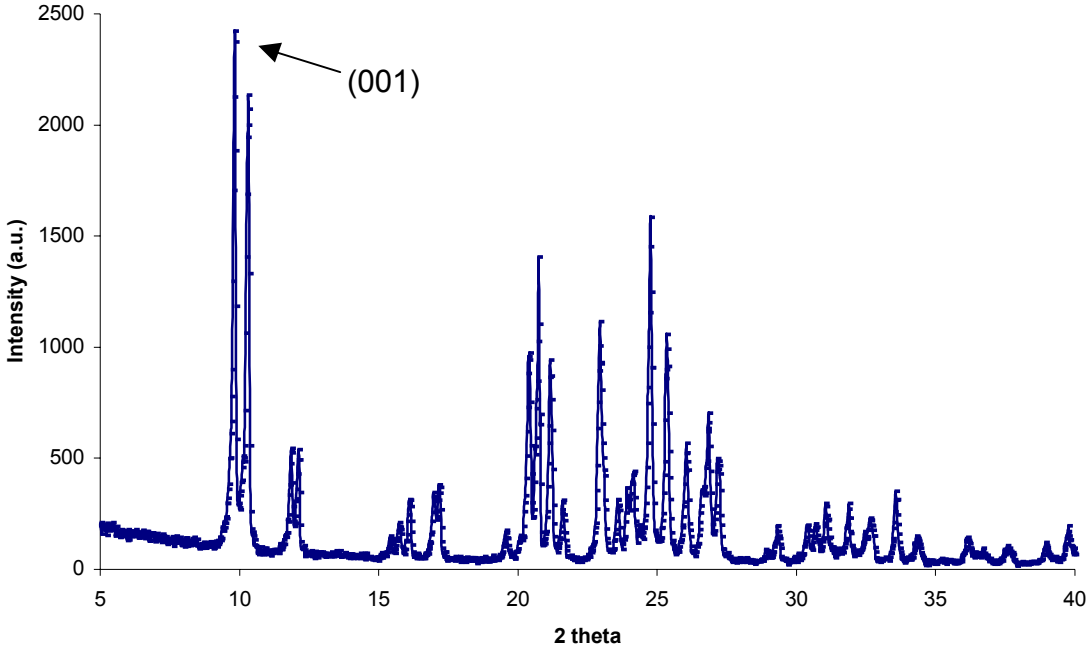

Figure 2.8 XRD pattern for as synthesized ALPO.

performing XRD at low angle for thin films to only reflect the structure that is present close to the surface of the film.

2.9 Transmission Electron Microscopy (TEM)

Results from TEM studies can confirm the dimensions of the distances obtained from XRD results. In this study, TEM images were collected with on the JEOL JEM-2000FXII Electron microscope operating at a voltage 200 kV. The samples were prepared by room temperature microtomy. Film samples were transferred into curing moulds and a few drops of epoxy (low temperature EXTEC curing resin) were poured over them. The samples were then allowed to cure for 3 to 5 hours at 45°C. The surface of the cross section containing the membrane was microtomed at 25°C using a Reichert ULTRACUT microtome equipped with a Diatome diamond knife to get Ultra-thin sections between 600 Å and 1000 Å.

2.10 Dynamic Mechanical Thermal Analysis (DMTA)

A Rheometric Scientific Mark IV DMTA was used to obtain physical properties on the nanocomposite i.e. the storage modulus (E'), the loss modulus (E''), the mechanical loss factor (tan δ), and the glass transition temperature (T_g). Experimental runs were performed on film samples having a length of 20 mm, a width of 6 mm, and a thickness of 0.06 mm. The run conditions were conducted

with a strain of 0.01%, a constant static force of 0.015N, and a heating rate of 3°C per minute in air.

Chapter 3 Gas Transport and Physical Property Testing

3.1 Visual Observations

Visual changes were observed when comparing a pure 6FDA-6FpDA-8%-DABA membrane with a 6FDA-6FpDA-8%-DABA membrane that contained 10% layered-ALPO. The membrane with the layered ALPO appeared homogenous throughout suggesting that the layered ALPO became well dispersed during the mixing process, however, it was visually more opaque. Both membrane samples were equally flexible and durable.

3.2 XRD; Results and Discussion

Figure 3.1 depicts the XRD patterns for as-synthesized ALPO (a) and swollen layered ALPO (b) without any polyimide. It can be seen that when comparing the as-synthesized ALPO to the layered-ALPO there is a clear peak shift from $2\theta=9.75$ to $2\theta=2.5$ in the (001) basal reflection. When applying the

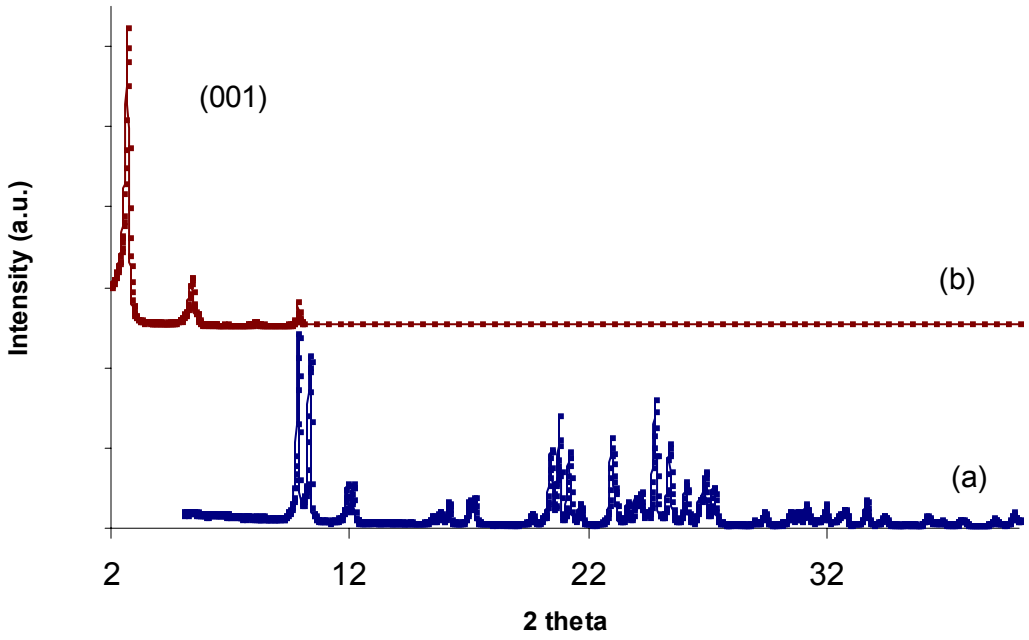

Figure 3.1 XRD patters of (a) as-synthesized layered ALPO and (b) swollen layered ALPO.

angles to Bragg's Law, the layers separated from a distance of 9.1 Å for the as synthesized layered ALPO to 31 Å for the swollen layered ALPO. This proves that the ALPO layers did indeed separate by the swelling process.

Figure 3.2 depicts the XRD patterns for (a) as-synthesized layered ALPO, (b) swollen layered ALPO, (c) the pure polyimide, and the (d) 10 wt% layered ALPO/polyimide nanocomposite; the latter two are in the form of thin films. Conclusions were drawn when comparing the XRD patterns of the swollen layered ALPO with the 10 wt% layered ALPO/polyimide nanocomposite. There is a broad peak at low angle in the 10 wt% layered ALPO/polyimide nanocomposite that does not correspond to the basal spacing of the swollen layered ALPO which suggests that the swollen layered ALPO are modified by the polyimide. When comparing this broad peak to the (001) reflection of the swollen layered ALPO indicates that a wide range of basal spacings exists ranging between 25 Å to 60 Å. This range of spacings along with the absence of higher angle reflections leads to a conclusion that the polymer protruded, intercalated, and exfoliated the layered ALPO. A ratio of how much intercalation or exfoliation actually occurred based on percentage is not known exactly. A similar broad peak has been seen before between poly(ethylene terephthalate)/montmorillonite clay nanocomposites, where the authors reached the same conclusion [52].

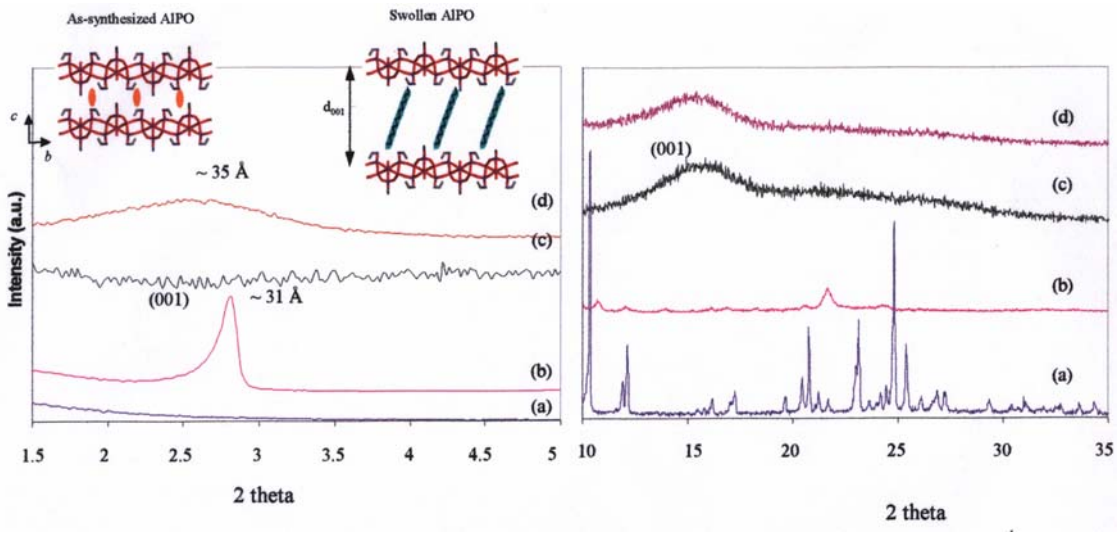

Figure 3.2. XRD patterns for (a) as-synthesized ALPO, (b) swollen layered ALPO, (c) the pure polyimide, and (d) the 10 wt% layered ALPO – polyimide nanocomposite.

3.3 Thermogravimetric Analysis (TGA)

TGA was performed at the University of Massachusetts to determine the extent of swelling. It was determined that only 32% of the cetyltrimethylammonium cation exchanged with the ethylamine cation during the swelling process.

3.4 TEM Studies

Figures 3.3 and 3.4 further depict evidence of intercalation and exfoliation of the layered ALPO in the 10 wt% nanocomposite membrane. The dark "whiskers" in the images correspond to single layers or a stack of few closely spaced layers intercalated with the polyimide. Spacings range from 25 to 90 Å, which is consistent with the broad peak observed in the XRD pattern seen in Figure 3.2(d). Although TEM images reveal layered ALPO oriented in the perpendicular direction, as is desired if these materials are to be used as membranes, there was also evidence of the layers being oriented parallel to the cross-section. This suggests that the layer orientation could be improved.

3.5 Gas Transport

Gas permeation experiments were performed to determine the effects of adding layered ALPO on gas transport properties of nanocomposite membranes. The permeability and selectivity coefficients for the pure polyimide, 5 wt% layered

ALPO, and 10 wt% layered ALPO, all mix blended for 4 days at 25˚C, are plotted in Tables 3.1 and 3.2 respectively. An additional 10% layered ALPO sample was also mix blended for 4 days at 55˚C, and its permeabilities and selectivitiy coefficients are compared in Tables 3.3 and 3.4. The permeabilities decreased as the weight percentage of layered ALPO increased, and the selectivitiy coefficients, in general, increased. The permeabilities and selectivities are plotted in Figures 3.5 through 3.9 and compared to Robeson's 1991 "upper bound"[4]. Figure 3.8 shows that the 10% layered ALPO caused the permeabilities and selectivities of the O_2-N_2 gas pair to exceed Robeson's 1991 upper bound.

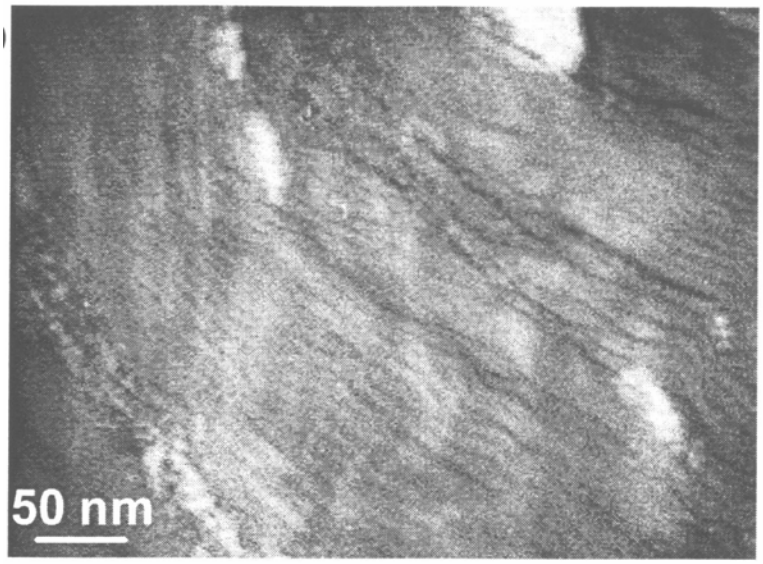

Figure 3.3 Intercalated and exfoliated polyimide – layered ALPO.

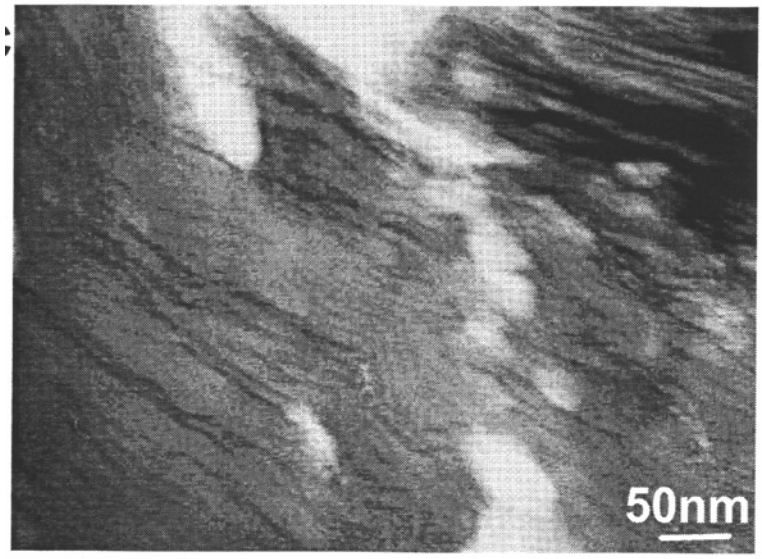

Figure 3.4 Intercalated and exfoliated polyimide – layered ALPO.

Table 3.1 PPLA nanocomposite membrane performance (permeability) at 30 °C. Relative error ~4% for permeability.

Permeability*	Pure Polyimide (PI)	5 wt% Layered AlPO Nanocomposite	10 wt% Layered AlPO Nanocompsite
He	178.83	147.54	94.43
O_2	36.25	24.32	18.53
N_2	10.11	6.15	2.08
CH_4	6.24	3.55	1.24
CO_2	83.72	65.67	51.16

Permeability = $\frac{10^{-10} cm^3(STP) \cdot cm}{cm^2 \cdot s \cdot cmHg}$; All membranes were mix blended for 4 days at 25 °C.

Table 3.2 PPLA nanocomposite membrane performance (selectivity) at 30 °C. Relative error ~4% for selectivity.coefficients.

Selectivity	Pure Polyimide (PI)	5 wt% Layered AlPO Nancomposite	10 wt% Layered AlPO Nanocomposite
He/O_2	4.93	6.07	5.10
He/N_2	17.69	23.99	45.40
He/CH_4	28.66	41.56	75.54
He/CO_2	1.55	2.25	1.85
O_2/N_2	3.59	3.95	8.91
O_2/CH_4	5.81	6.85	14.82
N_2/CH_4	1.62	1.73	1.66
CO_2/O_2	2.31	2.70	2.76
CO_2/N_2	8.28	10.68	24.60
CO_2-CH_4	13.42	18.50	40.93

All membranes were mix blended for 4 days at 25 °C.

Table 3.3 PPLA nanocomposite membrane performance (permeability) at 30 °C. Relative error ~4% on permeability.

Permeability*	Pure Polyimide (PI)	10 wt% Layered AlPO Nanocompsite[A]	10 wt% Layered AlPO Nanocompsite[B]
He	178.83	94.43	67.46
O_2	36.25	18.53	9.26
N_2	10.11	2.08	1.23
CH_4	6.24	1.24	0.70
CO_2	83.72	51.16	28.27

Permeability = $\frac{10^{-10} cm^3 (STP) \cdot cm}{cm^2 \cdot s \cdot cmHg}$; This membrane was mix blended for 4 days at 25 °C[A], this membrane was mix blended for 4 days at 55 °C[B].

Table 3.4 PPLA nanocomposite membrane performance (selectivity) at 30 °C. Relative error ~4% on selectivity coefficients.

Selectivity	Pure Polyimide (PI)	10 wt% Layered AlPO Nanocomposite[A]	10 wt% Layered AlPO Nanocomposite[B]
He/O_2	4.93	5.10	7.28
He/N_2	17.69	45.40	54.69
He/CH_4	28.66	75.54	98.83
He/CO_2	1.55	1.85	2.39
O_2/N_2	3.59	8.91	7.51
O_2/CH_4	5.81	14.82	13.30
N_2/CH_4	1.62	1.66	1.77
CO_2/O_2	2.31	2.76	3.05
CO_2/N_2	8.28	24.60	22.92
CO_2/CH_4	13.42	40.93	40.58

These membrane was mix blended for 4 days at 25 °C[A], this membrane was mix blended for 4 days at 55 °C[B].

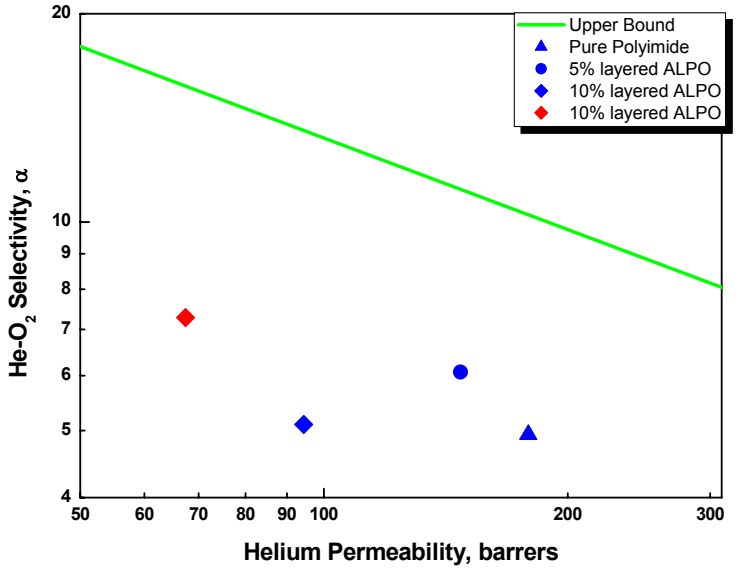

Figure 3.5. Boundary diagrams of 6FDA-6FpDA-DABA-8 pure polyimide and nanocomposite materials for selected gas pairs. The line represents Robeson's 1991 "Upper Bound".[7] The blue symbols represent mix blending for 4 days at 25°C and the red symbol represents mix blending for 4 days at 55°C.

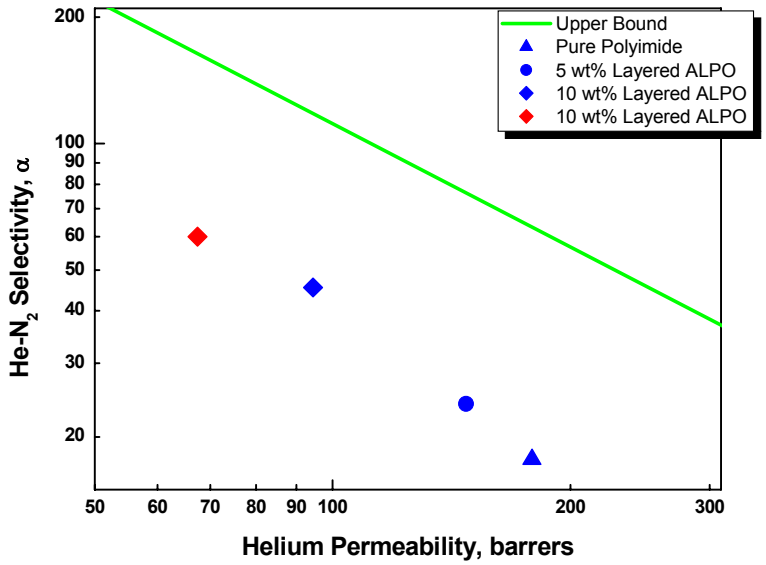

Figure 3.6. Boundary diagrams of 6FDA-6FpDA-DABA-8 pure polyimide and nanocomposite materials for selected gas pairs. The line represents Robeson's 1991 "Upper Bound".[7] The blue symbols represent mix blending for 4 days at 25°C and the red symbol represents mix blending for 4 days at 55°C.

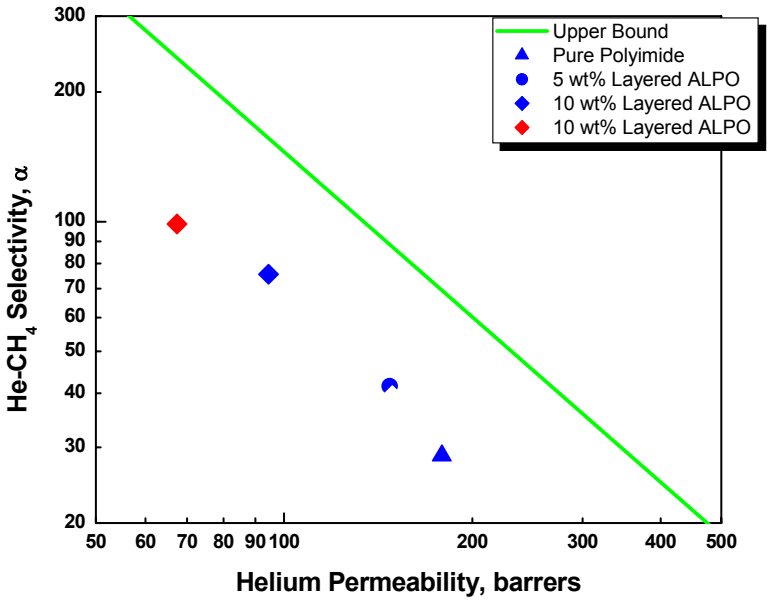

Figure 3.7. Boundary diagrams of 6FDA-6FpDA-DABA-8 pure polyimide and nanocomposite materials for selected gas pairs. The line represents Robeson's 1991 "Upper Bound".[7] The blue symbols represent mix blending for 4 days at 25°C and the red symbol represents mix blending for 4 days at 55°C.

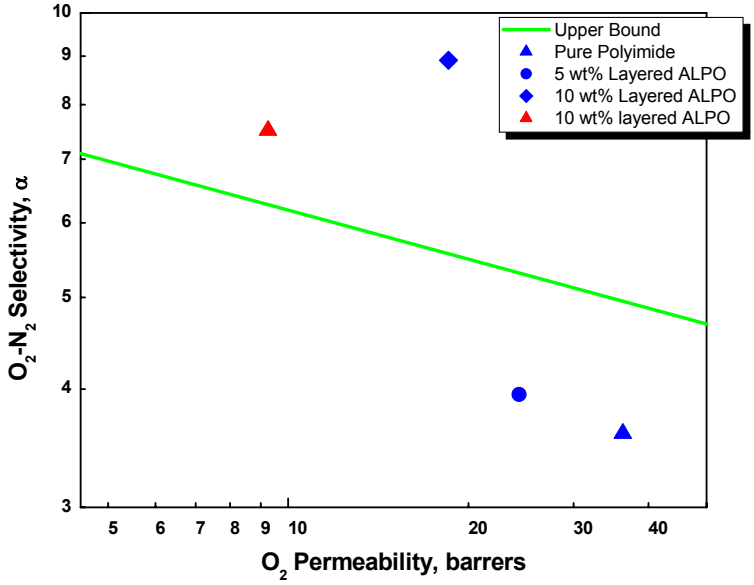

Figure 3.8. Boundary diagrams of 6FDA-6FpDA-DABA-8 pure polyimide and nanocomposite materials for selected gas pairs. The line represents Robeson's 1991 "Upper Bound".[7] The blue symbols represent mix blending for 4 days at 25°C and the red symbol represents mix blending for 4 days at 55°C.

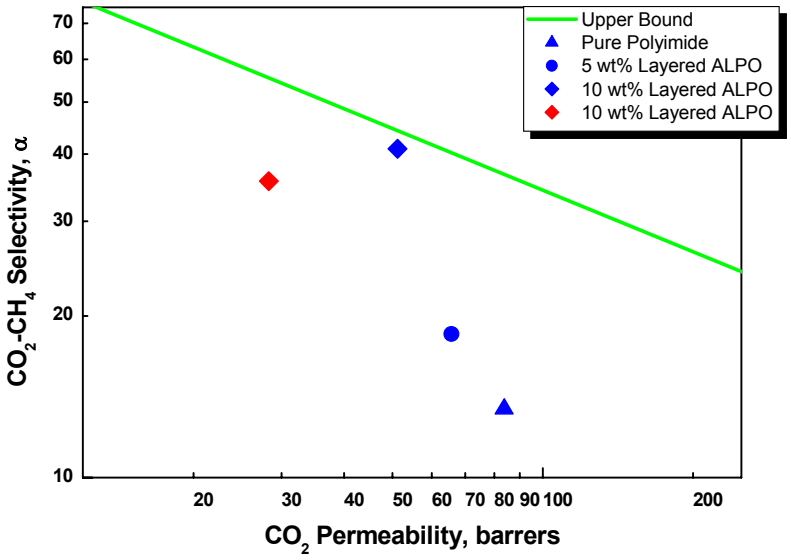

Figure 3.9. Boundary diagrams of 6FDA-6FpDA-DABA-8 pure polyimide and nanocomposite materials for selected gas pairs. The line represents Robeson's 1991 "Upper Bound" [7] The blue symbols represent mix blending for 4 days at 25°C and the red symbol represents mix blending for 4 days at 55°C.

3.6 Layered ALPO – Weight % Effects – Results & Discussion

The permeabilities and selectivity coefficients of a pure polyimide membrane are compared to permeabilities and selectivity coefficients of a 5 wt% and 10 wt% layered ALPO-polyimide nanocomposite membrane in Tables 3.1 and 3.2. The permeability decreases and the selectivity coefficients, in general, increase as the amount of layered ALPO increases from 5 wt% to 10 wt%. This phenomena may be explained by two different theories. The first involves the tortuous path of the diffusing molecule and the second involves the large interfacial volume of the nanocomposite [39].

The tortuous path mechanism theorizes that a layered sheet is non-permeable and that the diffusing species repeatedly changes its direction and therefore has a much longer path to diffuse through [39-41]. Equation 3.1 has been developed by Cussler to predict the permeability through such non-permeable layered sheets when incorporated in a nanocomposite [30].

$$P_{eff,\,i} / P_{p,\,i} = [1+\alpha^2 \phi^2 /(1-\phi)]^{-1} \qquad (3.1)$$

$P_{eff,\,i}$ is the effective permeability of species i, $P_{p,\,i}$ is the experimental permeability of species i, α is the aspect ratio, which is estimated at 1000 in this case and, ϕ is the volume fraction of the layered ALPO in the nanocomposite, which is 5% and 10% in this case. Equation 3.1 is most useful when these strongly anisotropic layered sheets are arranged with their short axis perpendicular to the film axis. Therefore, as the experimental permeability gets closer to the effective permeability, the more the layers are arranged perpendicular to the gas flow resulting in lower permeability. Similarly, equation

3.2 has been developed by Yano, Usuki, and Okada to predict the permeability through polyimide-clay hybrid films [9]. Equation 3.2

$$P_c/P_p = 1/(1+(L/2W)V_f) \qquad (3.2)$$

P_c is the permeability coefficient of the composite, P_p is the permeability coefficient of the polymer matrix, L is the length of a plate which, is assumed to be 1000, W is the with of a plate, which is assumed to be 1, and V_f is the volume fraction of a plate, which is 5% and 10% in this case. Equation 3.2 has been used to model water vapor permeating through polyimide-clay hybrid films, and assumes that all the clays are arranged perpendicular to the gas flow direction. The effective permeabilities from equation 3.1 and the permeability coefficients from equation 3.2 are compared with the experimental permeabilities in Tables 3.5 and 3.6. Since the differences in percentage between the effective permeabilities and experimental permeabilities are in the tens of thousands in Cussler's model, it can be concluded that most of these layered ALPO sheets are not arranged perpendicular to the gas flow, that exfoliation is incomplete, or that permeability occurs through the ALPO layers allowing the layered ALPO to act somewhat as a selective material.

Tables 3.5 and 3.6 also compare the aspect ratio of 100 and 1000 in the model by Yano, Usuki, and Okada with the experimental permeability. In both the 5 wt% layered ALPO and 10 wt% layered ALPO cases, the permeability coefficients are lower than the experimental permeability, but the experimental value is closer to the permeability coefficient when the aspect ratio is 100. By looking at the TEM image in Figure 3.3 the aspect ratio seems to be more like

Table 3.5 Effective permeability versus experimental permeability for 5 wt% layered ALPO nanocomposite. Relative error on experimental permeability ~4%.

Permeability Comparison	Effective Permeability for 5 wt% Layered ALPO (P_{eff})[A]	Permeability Coefficient for 5 wt% Layered ALPO (P_p)[B]	Experimental Permeability for 5 wt% Layered ALPO (P_p)
He (2.7 Å)	1.10, 68.7	6.53, 48.5	147.54
CO_2 (3.3 Å)	0.52, 32.2	3.06, 22.7	65.67
O_2 (3.4 Å)	0.22, 13.9	1.33, 9.84	24.32
N_2 (3.6Å)	0.06, 3.88	0.37, 2.74	6.15
CH_4 (3.9 Å)	0.03, 2.39	0.23, 1.69	3.55

Permeability = $\frac{10^{-10}\,cm^3(STP)\cdot cm}{cm^2\cdot s\cdot cmHg}$; model developed by Cussler[A]; model developed by Yano,

Usuki, and Okada[B]; aspect ratio α = 1000 and 100.

Table 3.6 Effective permeability versus experimental permeability for 10 wt% layered ALPO nanocomposite. Relative error on experimental permeability ~4%.

Permeability Comparison	Effective Permeability for 10 wt% Layered ALPO (P_{eff})[A]	Permeability Coefficient for 10 wt% Layered ALPO (P_p)[B]	Experimental Permeability for 10 wt% Layered ALPO (P_p)
He (2.7 Å)	0.27, 23.6	3.16, 26.8	94.43
CO_2 (3.3 Å)	0.13, 11.1	1.48, 12.6	51.16
O_2 (3.4 Å)	0.06, 4.80	0.64, 5.44	18.53
N_2 (3.6Å)	0.02, 1.33	0.18, 1.50	2.08
CH_4 (3.9 Å)	0.01, 082	0.11, 0.94	1.24

Permeability = $\frac{10^{-10}\,cm^3(STP)\cdot cm}{cm^2\cdot s\cdot cmHg}$; model developed by Cussler[A]; model developed by Yano,

Usuki, and Okada[B]; aspect ratio α = 1000 and 100.

1000 than 100. This reiterates the point that there is incomplete exfoliation, that the layers are not all perpendicular to gas flow, and that the layered ALPO is perhaps selective.

The theory that the ALPO is perhaps selective can be answered by comparing the permeability coefficient when the aspect ratio is 100 in Yano's model to the experimental permeability in Table 3.6. It can be seen that the permeability coefficient approaches the experimental permeability as the size of the gas gets larger. This suggests that for the smaller gases, He, CO_2, and O_2, the impermeable flakes model does not apply, and these ALPO layers are in fact size selective. However, it also suggests that for larger gases, N_2 and CH_4, the impermeable flakes model does apply concluding that the ALPO layers are not size selective for these gases.

3.7 Layered ALPO – Temperature Effects – Results & Discussion

As seen in Tables 3.3 and 3.4, the permeability is further reduced if the temperature of the polyimide-layered ALPO mix is blended at 55°C for 4 days. This suggests that there is more exfoliation in this 10 wt% layered ALPO membrane than in the 10 wt% layered ALPO membrane that was mixed at 25°C for 4 days. It is easier for this polyimide to protrude, intercalate, and eventually exfoliate this layered ALPO at a higher temperature. Therefore, it is suggested that as the temperature of the blending increases more exfoliation occurs. This

allows the polymer easier, more efficient, access to the space between the layers at a faster rate.

3.8 DMTA Analysis

It was desired to better understand the molecular interactions between the polymer and the layered ALPO by performing some mechanical testing via DMTA analysis.

The T_g, which was determined from the mechanical loss factor (tan δ), was compared between the pure polyimide and the nanocomposite. Figure 3.10 shows the relationship between the ratio of loss modulus to storage modulus and the temperature for the (a) pure polyimide, (b) the 10 wt% composite that was blended at 25°C, (c) the 10 wt% composite that was mix blended at 55°C, and (d) the10 wt% composite that was re-dissolved in THF, centrifuged, and then cast once again. Figure 3.11 is a plot showing the relationship between the ratio of loss modulus to storage modulus and the temperature for (a) the pure polyimide, (b) the 10 wt% composite that was mix blended at 55°C, and (c) a 3 wt% surfactant polyimide composite mix blended at 55°C. Figure 3.13 shows the storage modulus for the pure polyimide and the 10 wt% composite.

Figure 3.10 shows the ratio of the loss modulus to storage modulus between the pure polyimide and the nanocomposite; the peak is the T_g. Both the 10 wt% layered ALPO composite that was mix blended at 25°C and 55°C showed a “second” peak. This second peak can be attributed to another

component in the composite. When comparing the T_g of the pure polyimide of 322°C with the T_g of the 3 wt% surfactant sample of 318°C, in Figure 3.12, it can be suggested that a decrease in T_g is attributed to the surfactant. However, most of the decrease in T_g is due to the layered ALPO itself or some type of layered ALPO – surfactant – polyimide combination.

Also, Figure 3.10 proves that there is no degradation occurring in the sample because the ratio of the loss modulus to storage modulus of the pure polyimide was compared with a 10 wt% layered ALPO sample that was re-dissolved, centrifuged, and re-cast; the curves are identical.

In addition, Figure 3.10 proves that the large interfacial volume mechanism theory does not apply to these nanocomposites. This theory states that the large surface area of exfoliated ALPO sheets cause the majority of the polymer to lie close to the layered ALPO-polyimide interface. This restricts the mobility of the polymer and any molecules attempting to diffuse through the polymer. However, this is not the case here, because a decrease in T_g was measured rather than an increase, which would suggest reduced polymer mobility.

Figure 3.12 represents the storage modulus between the pure polyimide and the 10 wt% layered ALPO nanocomposite. The pure polyimide eventually drops off rapidly and fails at 370°C, but the nanocomposite drops off less rapidly, and never fails even at 500°C, suggesting eventual cross-linking.

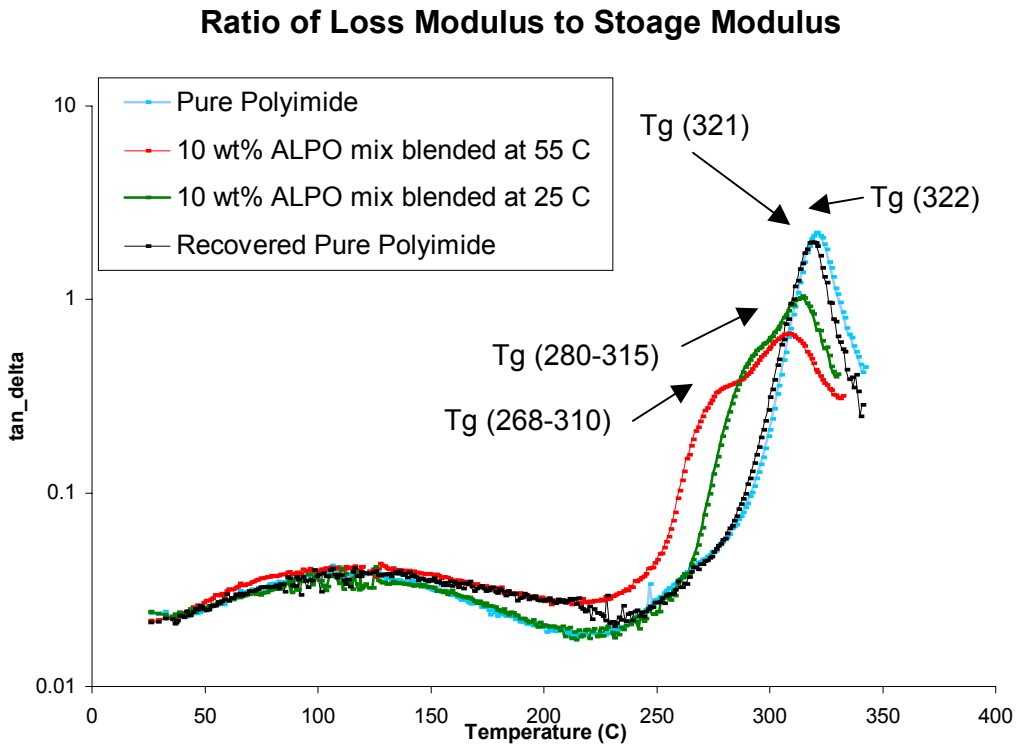

Figure 3.10. Ratio of loss modulus to storage modulus for (a) the pure polyimide, (b) 10 wt% ALPO; mix blended at 55 ° C, (c) 10% wt ALPO; mix blended at 25°C, and (d) the pure polyimide that was re-dissolved, centrifuged, and re-cast.

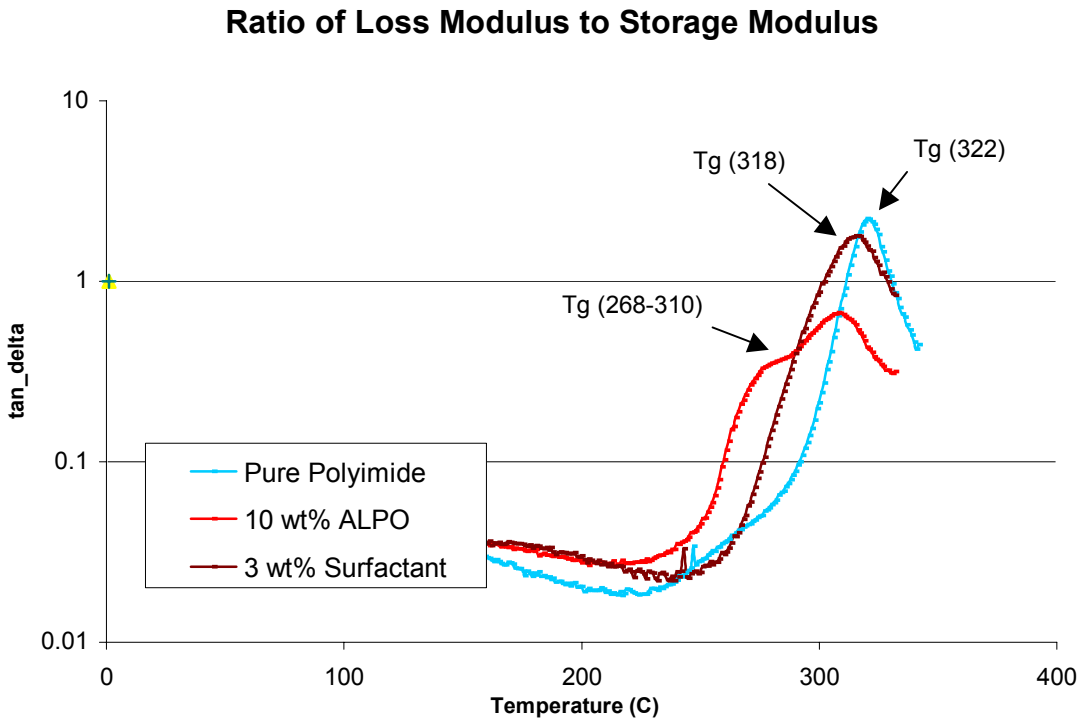

Figure 3.11. Ratio of loss modulus to storage modulus for (a) the pure polyimide, (b) the 10 wt% ALPO, (c) and a 3 wt% surfactant composite; all mix blended at 55°C.

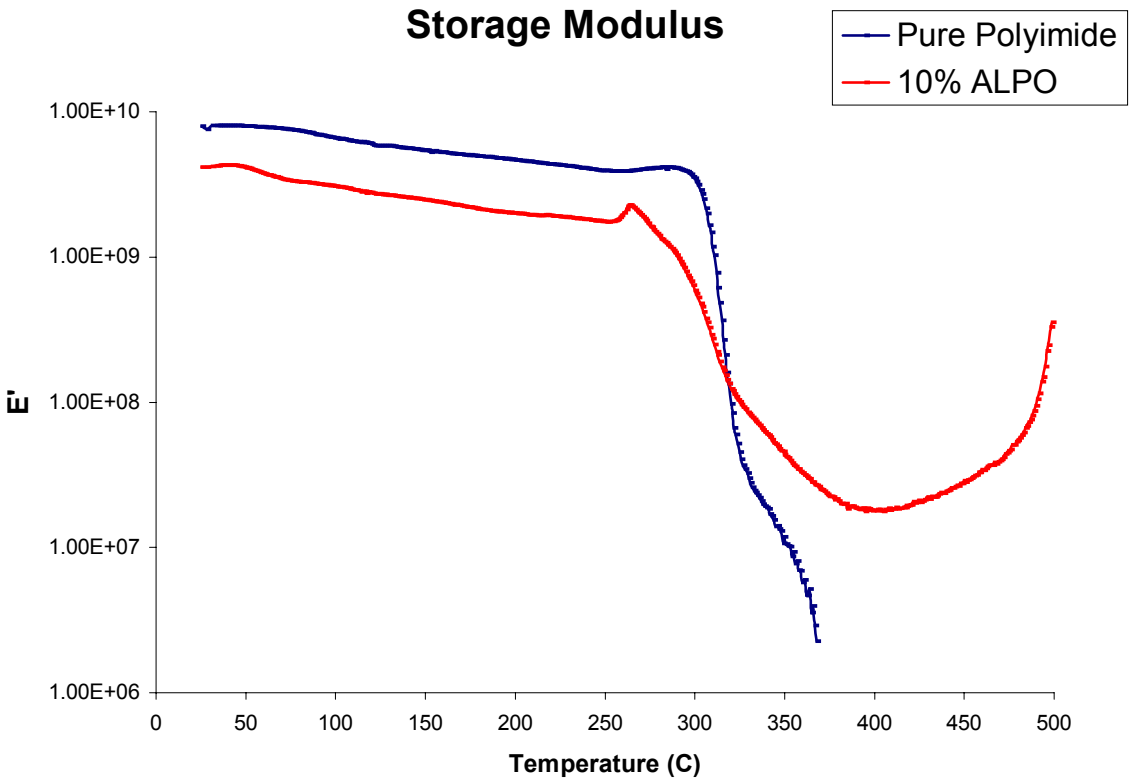

Figure 3.12. The storage modulus of the (a) pure polyimide and (b) the 10 wt% ALPO sample.

3.9 Conclusion

In conclusion, polyimide-layered ALPO membranes are synthesized and fabricated for the first time. The XRD patterns and TEM images show intercalation and some exfoliation of the polyimide into the layered ALPO. Dramatic decreases in permeabilities and increases in selectivity coefficients with an addition of 5 wt% and 10 wt% layered ALPO into the polyimide were observed, suggesting that the layered ALPO is selective. Simultaneous improvement in thermal stability was also demonstrated. The permeability and selectivity for the O_2/N_2 gas pair for 10 wt% layered ALPO exceeded Robeson's upper bound into the "commercially attractive" region.

Chapter 4 Recommendations

4.1 Future Work

To my knowledge, this is the first time that polyimide-layered ALPO membranes are fabricated. Although the selectivity coefficients improved when increasing the amount of layered ALPO, changing the pore size of the ALPO structure could further test the effect of size selectivity through the nanocomposite. In this research a 4 x 6 x 8 layered ALPO network was incorporated into the nanocomposite. A 4 x 8, 4 x 12, or 4 x 6 x 12 network should be incorporated into the polymer to determine if this helps selectivity improvements especially between larger gases i.e. N_2 and CH_4 [54-56]. The amount of selectivity improvement coming from the pore size of the ALPO and from the polymer needs to be determined by constructing various nanocomposite combinations by first keeping the pores size of the ALPO constant while varying the polymer based on T_g. Second, the pore size of the layered ALPO should be varied while holding the polymer constant. All of these combinations should be

analyzed to see if a trend develops so that a model for gas permeation through nanocomposites may be developed.

Experiments such as IR should be performed on these different polymer – pore size ALPO combinations to further understand hydrogen bonding forces, electrostatic forces, and cation-anion interactions at the polymer - layered ALPO interface. Also, high temperature annealing studies should be performed to determine if crosslinking occurs between the carboxylic acid group in the DABA and the layered ALPO.

Sorption studies on the polymer, ALPO, and the nanocomposite should be performed separately to further characterize and compare these materials. In particular, the temperature (35°C, 50°C, 65°C, etc.) versus pressure (4atm, 10 atm, 15 atm, etc.) should be plotted to obtain isotherms that would determine the sorption mechanism; currently permeation experiments are performed at low temperature (35°C) and pressure (4 atm). This sorption study would lead to a direct impact on the effective permeabilities obtained from Cussler's and Yano's models.

4.2 References

1. Ghosal, K.;Freeman, B.D. *Polymer for Advanced Technologies*, **1994**, *5*, 673.

2. Koros, W.J; Fleming, G.K. *J. Membr. Sci.*, **1993**, *83*, 1.

3. Baker, R.W. *Ind. Eng. Chem. Res*., **2002**, *41*, 1393.

4. Robeson, L.M. *J. Membr. Sci.*, **1991**, *62*, 165.

5. Pechar, T.W.; Tsapatsis, M.; Marand, E.; Davis, R. Desalination, **2002**, *156*, 3.

6. Zhu, Z, ; Yang, Y.; Yin, J.; Wang, X.; Ke, Y.; Qi, Z. *J. Appl. Polym. Sci*., **1998**, *73*, 2063.

7. Alexandre, M.; Dubois, P*. Mat. Sci. Eng*., **2000**, *28*, 1.

8. Alexandre, M.; Beyer, G.; Henrist, C.; Cloots, R.; Rulmont, A.; Jerome, R.; Dubois, P. *Macromol. Rapid Commun*., **2001**, *22*, 643.

9. Hwu, J.M.; Jiang, G.; Gao, Z.M.; Xie, W.; Pan, W.P. *J. Appl. Polym. Sci*., **2001**, *83*, 1702.

10. Yano, K.; Usuki, A.; Okada, A. *J. Polym. Sci. A: Polym. Chem*., **1997**, *35*, 2289.

11. Yang, Y.; Zhu, Z.; Yin, J.; Wang, X.; Qi, Z. *Polymer*, **1999,** *40*, 4407.

12. Carrado, K.A. *Appl. Clay Sci*., **2000**, *17*, 1.

13. Kornmann, X. Synthesis and Characterization of Thermoset-Layered Silicate Nanocomposites. Ph.D. Dissertation, Lulea University of Technology, March 2001

14. Kornmann, X.; Lindberg, H.; Berglund, L.A*. Polymer*, **2001**, *42*, 1303.

15. Yano, K.; Usuki, A.; Okada, A.; Kurauchi, T.; Kamigaito, O. *J. Polym. Sci. Part A Polym. Chem*., **1993**, *31*, 2493.

16. Kojima, Y.; Usuki, A.; Kawasami, M.; Okada, A.; Kurauchi, T.; Kamigaito,O.; *J. Polym. Sci. Part A Polym. Chem.,* **1993**, *31*, 983.

17. Kojima, Y.; Usuki, A.; Kawasami, M.; Okada, A.; Kurauchi, T.; Kamigaito,O.; *J. Appl. Polym. Sci.,* **1993**, *49*, 1259.

18. Kojima, Y.; Fukumori, K.; Usuki, A.; Kawasami, M.; Okada, A.; Kurauchi, T. *J. Mater Sci. Lett.,* **1993**, *12*, 889.

19. Kojima, Y.; Usuki, A.; Kawasami, M.; Okada, A.; Kurauchi, T.; Kamigaito,O.; *J. Mater Res.,* **1993**, *8*, 1185.

20. Ke, Y.C.; Qi, Z.N.; In Proceedings of the 1997 Chinese National Symposium on Polymers, Hefei, Oct. 1997; pf101.

21. Ke, Y.C.; Qi, Z.N.; In Proceedings of the 1997 Chinese National Symposium on Polymers, Hefei, Oct. 1997; pf103.

22. Ke, Y.C.; Qi, Z.N.; In Proceedings of the 1997 Chinese National Symposium on Polymers, Hefei, Oct. 1997; pf107.

23. Cornelius, C.J.; Marand, E. *Polymer*, **2002**, *43*, 2385.

24. Cornelius, C.J.; Marand, E. *J. Membr. Sci.*, submitted May **2001**.

25. Cornelius, C.J.; Hibshman, C.; Marand, E. *Sep. Purif. Technol.*, **2001**, *25*, 181.

26. Cornelius, C.J. Hybrid Inorganic-Organic Materials: Physical and Gas Permeation Properties for a Series of Fluorinated Polyimide Composites. Ph.D. Dissertation, Virginia Polytechnic Institute and State University, July **2000**.

27. Alexopoulos, J.B.; Barrie, J.A.; Machin, D. *Polymer*, **1969**, *10*, 265.

28. Frisch, H.L. *Polymer Journal*, **1991**, *23*, 445.

29. Vasak, F.; Broz, Z. *J. Membr. Sci.*, **1993**, *82*, 265.

30. Cussler, E.L., "Diffusion. Mass Transfer in Fluid Systems," 2nd edition, Cambridge, 1997, p.174-175.

31. Paul, D.R. *J. Polym. Sci. Part A-2,* **1969**, *7*, 1811.

32. Paul, D.R.; Kemp, D.R. *J. Polym. Sci.: Symposium No. 41*, **1973**, 79.

33. Zimmerman, C.M.; Singh, A.; Koros, W.J. *J. Polym. Sci.: Part B: Poly. Phys.*, **1998**, *36*,1747.

34. Wessling, M.; Schoeman, S.; van der Boomgaard, Th; Smolders, C.A. *Gas Sep. and Purif.*, **1991**, *5*, 222.

35. Beall, G.W.; Kamena, K. *Proceedings Antec 1999* Soc. Plast. Eng.; Brookfield, CT; Vol. III, 3937

36. Giannelis, E.P. *Adv Mater.*, **1996**, *8*, 29

37. Vaia, R. A.; Giannelis, E.P. *Macromolecules*, **1997**, *30*, 8000

38. Stockmeyer, M.R. *Applied Clay Science*, **1991**, *6*, 39

39. Vaia, R.A.; Price, G.; Ruth, P.N.; Nguyen, H.T.; Lichtenham, J.; *Applied Clay Science*, **1999**, *15*, 67

40. Kornmann, X.; Berglund, L.A.; Sterte, J.; *Polym. Eng. And Sci.*, **1998**, *38*, 8

41. Vaia, R.A; Ishii, H.; Giannelis, E.P.; *Chem. Mater.*, **1993**, *5*, 1694

42. Burnside, S.D.; Wang, H.; Giannelis, E.P.; *Chem. Mater.*, **1999**, *11*, 1055

43. Vaia, R.A.; Jandt, K.D.; Kramer, E.J.; Giannelis, E.P.; *Chem. Mater.*, **1996**, *8,* 2628

44. Vaia, R.A.; Giannelis, E.P; *Macromolecules*, **1997**, *30*, 7990

45. Yano, K.; Usuki, A.; Okada, A.; Kuraychi, T; Kamigaito, O.; *Polym. Sci.; Polym. Chem.*, **1993***, 31*, 2493

46. Gao, Q.; Li, B.; Chen, J.; Li, S.; Xu, R.; *J. Solid State Chem.*, **1997**, *129*, 37

47. Corma, A.; Fornes, V.; Pergher, S.B.; Maesen, Th.L.M.; Buglass, J.G.; *Nature*, **1998**, *396*, 353

48. Corma, A.; Fornes, V.; Martinez-Triguero, J.; Pergher, S.B.; *J. Catal.*, **1999**, *186*, 57

49. Chan, F.C; Anwar,J; Cernik, R.; Barnes, P.; Wilson, R.M.; *J. Appl. Crystallogr.*, **1999**, *32*, 436

50. Kokotailo, G.T.; Lawton, S.L.; *Nature*, **1978**, *272*, 437

51. Deem, M.W.; Newsam, J.M.; *Nature*, **1989**, *342*, 260

52. Brenner, S.; *Ph.D. Thesis*, ETH, Zurich, Switzerland

53. Davis, C.H.; Mathias, L.J.; Gilman, J.W.; Schiraldi, D.A.; Shields, J.R.; Trulove, P.; Sutto, T.E.; Delong, H.C.; *J. Polym. Sci.: Part B: Poly. Phys*, **2002**, *40*, 2661.

54. Vidal, L.; Marichal, C.; Gramlich, V.; Patarin, J.; Gabelica, Z*.; Chem. Mater*, **1999**, *11*, 2728.

55. Wei, B.; Yu, J.; Qui, S.; Li, J.; *J. Chem. Soc., Dalton Trans*., **2000**, 1979.

56. Huang, Q.; Hwu, S; *Chem Mater*, **2001**, *13*, 1794.

Vita

The author was born in Lodz, Poland on April 17, 1978. Wojtek came to the United States in November of 1982 and gained citizenship in May of 1990. After graduating from Glencliff High School in Nashville, TN, Wojtek attended Tennessee Technological University where he earned the degree of Bachelors of Science in Chemical Engineering in May of 2001. With an interest in polymers, the author began his graduate studies at Virginia Polytechnic Institute and State University under the direction of Dr. Eva Marand. Wojtek successfully defended his Masters Thesis in June of 2003.